Author for correspondence:
Mengsen Zhang
e-mail: mengsenz@stanford.edu

[†]Present address: Department of Psychiatry and Behavioral Sciences, Stanford University, Stanford, CA, USA.

THE ROYAL SOCIETY
PUBLISHING

Connecting empirical phenomena and theoretical models of biological coordination across scales

Mengsen Zhang[1,†], Christopher Beetle[2], J. A. Scott Kelso[1,3] and Emmanuelle Tognoli[1]

[1]Center for Complex Systems and Brain Sciences, and [2]Department of Physics, Florida Atlantic University, Boca Raton, FL, USA
[3]Intelligent Systems Research Centre, Ulster University, Derry~Londonderry, Northern Ireland

MZ, 0000-0003-3085-152X

Coordination in living systems—from cells to people—must be understood at multiple levels of description. Analyses and modelling of empirically observed patterns of biological coordination often focus either on ensemble-level statistics in large-scale systems with many components, or on detailed dynamics in small-scale systems with few components. The two approaches have proceeded largely independent of each other. To bridge this gap between levels and scales, we have recently conducted a human experiment of mid-scale social coordination specifically designed to reveal coordination at multiple levels (ensemble, subgroups and dyads) simultaneously. Based on this experiment, the present work shows that, surprisingly, a single system of equations captures key observations at all relevant levels. It also connects empirically validated models of large- and small-scale biological coordination—the Kuramoto and extended Haken–Kelso–Bunz (HKB) models—and the hallmark phenomena that each is known to capture. For example, it exhibits both multistability and metastability observed in small-scale empirical research (via the second-order coupling and symmetry breaking in extended HKB) and the growth of biological complexity as a function of scale (via the scalability of the Kuramoto model). Only by incorporating both of these features simultaneously can we reproduce the essential coordination behaviour observed in our experiment.

1. Introduction

Coordination is central to living systems and biological complexity at large, where the whole can be more than and different from the sum of its parts. Rhythmic coordination [1–3] is of particular interest for understanding the formation and change of spatio-temporal patterns in living systems, including, e.g. slime mould [4,5], fireflies [6,7], social groups [8,9] and the brain [10–14]. Theoretical descriptions of biological coordination are often in terms of coupled oscillators, whose behaviour is constrained by their phase relations with each other [2,15–18]. Existing studies of phase coordination often focus on systems of either very few (small-scale, mostly $N = 2$) [13,19,20], or very many oscillators (large-scale, $N \to \infty$) [21–23]. Here we inquire how the two might be connected and applied to midscale systems with neither too many nor too few components. The present work answers this question by modelling empirically observed coordinative behaviour in midscale systems ($N = 8$), based on data collected in a specially designed human experiment [24]. The resultant model that captures all key experimental observations happens to also connect previous theories of small- and large-scale biological coordination in a single mathematical formulation.

But first, how are small- and large-scale models different? Small-scale models were usually developed to capture empirically observed coordination patterns, as in animal gaits [25–27], bimanual movement coordination [28,29], neuronal coordination [30], interpersonal coordination [31,32], human–animal coordination [33] and human–machine coordination [34,35]. They describe multiple stable coordination patterns (multistability) and the transitions between them (order-to-order transitions), e.g. from a trot to a gallop for a horse [36]. In humans, dyadic coordination patterns like inphase and antiphase (synchronization, syncopation) were found across neural, sensorimotor and social levels (see [13,14] for reviews), well captured by the extended Haken–Kelso–Bunz (HKB) model [29,37,38]. However, the extended HKB was restricted to describing coordination phenomena at $N = 2$ (i.e. not directly applicable to higher-dimensional coordination phenomena). By contrast, large-scale models are concerned more about statistical features like the overall level of synchrony and disorder-to-order transitions, but not so much about patterns at finer levels. As a representative, the classical Kuramoto model [2] is applicable to describing a wide range of large-scale coordination between, e.g. people [23,39], fish [40] and neural processes [22], and is often studied analytically for its incoherence-to-coherence transition (at the statistical level, for $N \to \infty$; see [41,42] for reviews).

Although the extended HKB and the classical Kuramoto model emerged separately, they connect to each other by an interesting difference: the Kuramoto model with $N = 2$ is *almost* the extended HKB model except that the former lacks the term responsible for antiphase coordination in the latter (more accurately, the bistability of inphase and antiphase). Bistability of inphase and antiphase coordination, with associated order-to-order transitions and hysteresis, happens to be a key observation in small-scale human experiments [28,43]. This begs the question of whether there is a fundamental difference between large- and small-scale coordination phenomena. Does the existence of antiphase, multistability, and order-to-order transitions depend on scale N? With these questions in mind, we recently conducted a human experiment [24] at an intermediate scale ($N = 8$), such that the system is large enough for studying its macro-level properties, yet small enough for examining patterns at finer levels, ideal for theories and empirical data to meet at multiple levels of description. In the following sections, we demonstrate how the marriage between the two models (not either one alone) is sufficient for capturing empirical observations at multiple levels of description and we discuss its empirical and theoretical implications for biological coordination.

2. Results

2.1. Human coordination at intermediate scales

Before getting into the model, we briefly review the mid-scale experiment and key results [24]. In the experiment (dubbed the 'Human Firefly' experiment), ensembles of eight people ($N = 8$, total 120 subjects) spontaneously coordinated rhythmic movements in an all-to-all network (via eight touchpads and eight ring-shaped arrays of eight LEDs as in figure 1; see Material and methods for details), even though they were not explicitly instructed to coordinate with each other. To induce different grouping behaviour, subjects were paced with different metronomes prior to interaction such that each

ensemble was split into two frequency groups of equal size with intergroup difference $\delta f = 0$, 0.3 or 0.6 Hz (referred to as levels of 'diversity'), and were asked to maintain that frequency during interaction after the metronome was turned off. Subjects' instantaneous tapping frequencies from three example trials (figure 2a–c) show intuitively the consequences of frequency manipulations: from (a) to (c) a supergroup of eight gradually split into two frequency groups of four as diversity increased from $\delta f = 0$ to 0.6 Hz.

Key results involve multiple levels of description, in terms of intergroup, intragroup and interpersonal relations. The level of intergroup integration is defined as the relationship between intragroup and intergroup coordination (β_1, slope of regression lines in figure 3a. Here intragroup coordination is measured by the average pair-wise phase-locking value over all intragroup dyads, and likewise, intergroup coordination over all intergroup dyads. Phase-locking value *per se* is a measure of stability of a relative phase pattern within a period of time, which equals to one minus the circular variance. See section 'Phase-locking value and level of integration' for technical details). Intuitively, we say that two groups are integrated if intragroup and intergroup coordination facilitate each other (positive relation between respective phase-locking values, $\beta_1 > 0$), and segregated if intragroup and intergroup coordination undermine each other (negative relation between respective phase-locking values, $\beta_1 < 0$. We will see later in figure 4 how this measure meaningfully captures coordination dynamics). In the experimental result, two frequency groups were integrated when diversity is low or moderate ($\delta f = 0$, 0.3 Hz, blue and red lines, slope $\beta_1 > 0$) and segregated when diversity is high ($\delta f = 0.6$ Hz, yellow line, slope $\beta_1 < 0$). A critical level of diversity demarcating the regime of intergroup integration and segregation was estimated to be $\delta f^* = 0.5$ Hz. Within the frequency groups, coordination was also reduced by the presence of intergroup difference (figure 3b, left, red and yellow bars shorter than blue bar). At the interpersonal level, inphase and antiphase were preferred phase relations (inphase much stronger than antiphase; distributions in figure 2d–f), especially when the diversity was very low (figure 2d, peaks around $\phi = 0$, π, in *radians* throughout this paper), but both were weakened by increasing diversity (figure 2e,f; in episodes of strong coordination, antiphase is greatly amplified and much more susceptible to diversity than inphase, see [24]). Notice that subjects did not remain locked into these phase relations but rather engaged and disengaged intermittently (two persons dwell near and escape from preferred phase relations recurrently, a sign of metastability [13]; see figure 6a red trajectory for example), reflected also as 'kissing' and 'splitting' of frequency trajectories (e.g. in figure 2b). In the following sections, we present a model that captures these key experimental observations at their respective levels of description.

2.2. A minimal experiment-based model of multiagent coordination

Our model of coordination is based on a family of N oscillators, each represented by a single phase angle φ_i. We will show that a pair-wise phase coupling [2,25,29] of the form

$$\dot{\varphi}_i = \omega_i - \sum_{j=1}^{N} a_{ij} \sin(\varphi_i - \varphi_j) - \sum_{j=1}^{N} b_{ij} \sin 2(\varphi_i - \varphi_j), \quad (2.1)$$
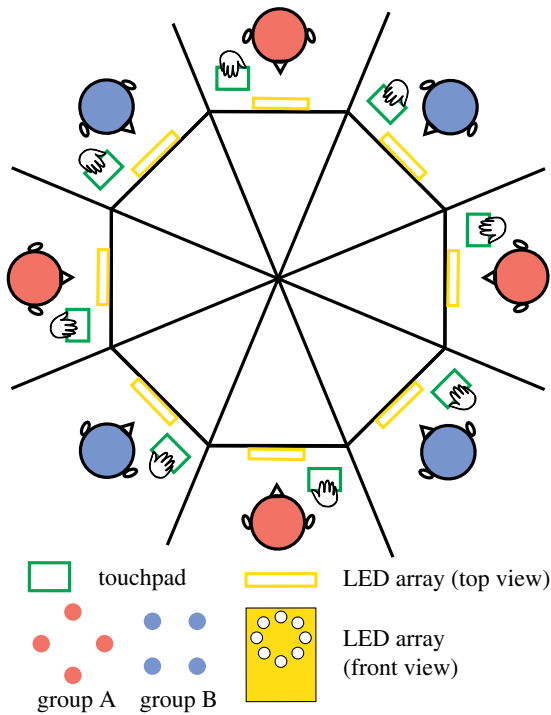
Figure 1. Experimental set-up for multiagent coordination. In the Human Firefly experiment [24], eight subjects interacted simultaneously with each other via a set of touch pads and LED arrays. Each subject's movements were recorded with a dedicated touchpad. Taps of each subject were reflected as the flashes of a corresponding LED on the array presented in front of each subject. In each trial, each subject was paced with a metronome prior to interaction. The metronome assignment split the ensemble of eight into two frequency groups of four (group A and B, coloured red and blue, respectively, for illustrative purposes; the actual LEDs are all white). The frequency difference δf between group A and B was systematically manipulated to induce different grouping behaviour. See text and [24] for details. (Online version in colour.)

suffices to model the key features of the experimental data identified above. The left side of this equation is the time derivative of φ_i, while the constant $\omega_i > 0$ on the right is the natural (i.e. uncoupled) frequency of the ith oscillator. The coefficients $a_{ij} > 0$ and $b_{ij} > 0$ are parameters that govern the coupling.

Equations (2.1) include a number of well-studied models as special cases. For instance, setting $\phi := \varphi_1 - \varphi_2$, $\delta\omega := \omega_1 - \omega_2$, $\tilde{a} := a_{12} + a_{21}$ and $2\tilde{b} := b_{12} + b_{21}$ for $N = 2$, the difference of the two resulting equations (2.1) yields the relative phase equation

$$\dot{\phi} = \delta\omega - \tilde{a}\sin\phi - 2\tilde{b}\sin 2\phi, \qquad (2.2)$$

of the extended HKB model [37]. The HKB model [29] was originally designed to describe the dynamics of human bimanual coordination, corresponding to equation (2.2) with $\delta\omega = 0$ (i.e. describing the coordination between two identical components). The extended HKB introduces the symmetry breaking term $\delta\omega$ to capture empirically observed coordinative behaviour between asymmetric as well as symmetric components (i.e. the HKB model is included in the extended HKB model, which is further included in equations (2.1)). It has since been shown to apply to a broad variety of dyadic coordination phenomena in living systems, e.g. [13,14,19,43,44]. Equations (2.1) can be considered a generalization of the extended HKB model from 2 to N oscillators.

It is remarkable that such a direct generalization can reproduce key features of the collective rhythmic coordination in *ensembles* of human subjects at *multiple* levels of description.

Another well-studied special case of equations (2.1) is the Kuramoto model [2], which has $b_{ij} = 0$ (and typically $a_{ij} = a$, independent of i and j). We will see below, however, that the Kuramoto model cannot exhibit at least one feature of the experimental data. Namely, the data show a secondary peak in the pairwise relative phase of experimental subjects at antiphase (see figure 2d–f). Simulations using the Kuramoto model do not reproduce this effect, while simulations of equations (2.1) model do (compare figure 5d–f and g–i). We give additional analytical support for this point by studying relevant fixed points of both models in the electronic supplementary materials (section 'Multistability of the present model').

2.3. Weak coupling captures human behaviour

Given the spatially symmetric set-up of the 'Human Firefly' experiment (all-to-all network, visual presentation at equal distance to fixation point), it is reasonable to further simplify equations (2.1) by letting $a_{ij} = a$ and $b_{ij} = b$ (a, $b > 0$),

$$\dot{\varphi}_i = \omega_i - a\sum_{j=1}^{N}\sin\phi_{ij} - b\sum_{j=1}^{N}\sin 2\phi_{ij}, \qquad (2.3)$$

where $\phi_{ij} = \varphi_i - \varphi_j$ is the relative phase between oscillators i and j (henceforth we use the notation ϕ_{ij} instead of the subtraction, since relative phase is the crucial variable for coordination [28,29]).

The behaviour of the model itself clearly depends on the coupling strength (a, b) and frequency diversity (distribution of ω_i's). While the latter was explicitly manipulated in the human experiment [24], the former was unknown. A qualitative look at simulated dynamics (see examples figure 4a–c for $\delta f = 0.6$ Hz) indicates that weak coupling better captures human behaviour (members of the same group do not collapse to a single trajectory in figure 4a as in figure 2). By contrast, stronger coupling (figure 4b,c) deprives the system of much of the metastability. Quantitatively, we fitted the coupling strength (assuming $a = b$) to the human data based on the level of intergroup integration (β_1) (see distribution of model β_1 in figure 4d) particularly for diversity condition $\delta f = 0.3$ Hz (i.e. using only one-third of the data to prevent overfitting). We show below how the model captures human behaviour across all diversity conditions and levels of description under the best-fit coupling strength ($a = b = 0.105$; see section 'Choosing the appropriate coupling strength' in the electronic supplementary materials for more details).

At the level of intergroup relations, model behaviour (figure 3c) successfully captures human behaviour (figure 3a) at all levels of diversity. Similar to the human experiment, low diversity ($\delta f = 0$ Hz) results in a high level of integration in the model (blue line in figure 3c slope close to 1; $\beta_1 = 0.972$, $t_{199} = 66.6$, $p < 0.001$); high diversity ($\delta f = 0.6$ Hz) comes with segregation (yellow line slope negative; $\beta_1 = -0.113$, $t_{199} = -3.56$, $p < 0.001$); and in between, moderate diversity ($\delta f = 0.3$ Hz) is associated with partial integration (red line positive slope far less than 1; $\beta_1 = 0.318$, $t_{199} = 4.23$, $p < 0.001$). Here we did not estimate the critical diversity δf^* the same way as for the human data (by linear interpolation), since we found theoretically that the level of integration depends
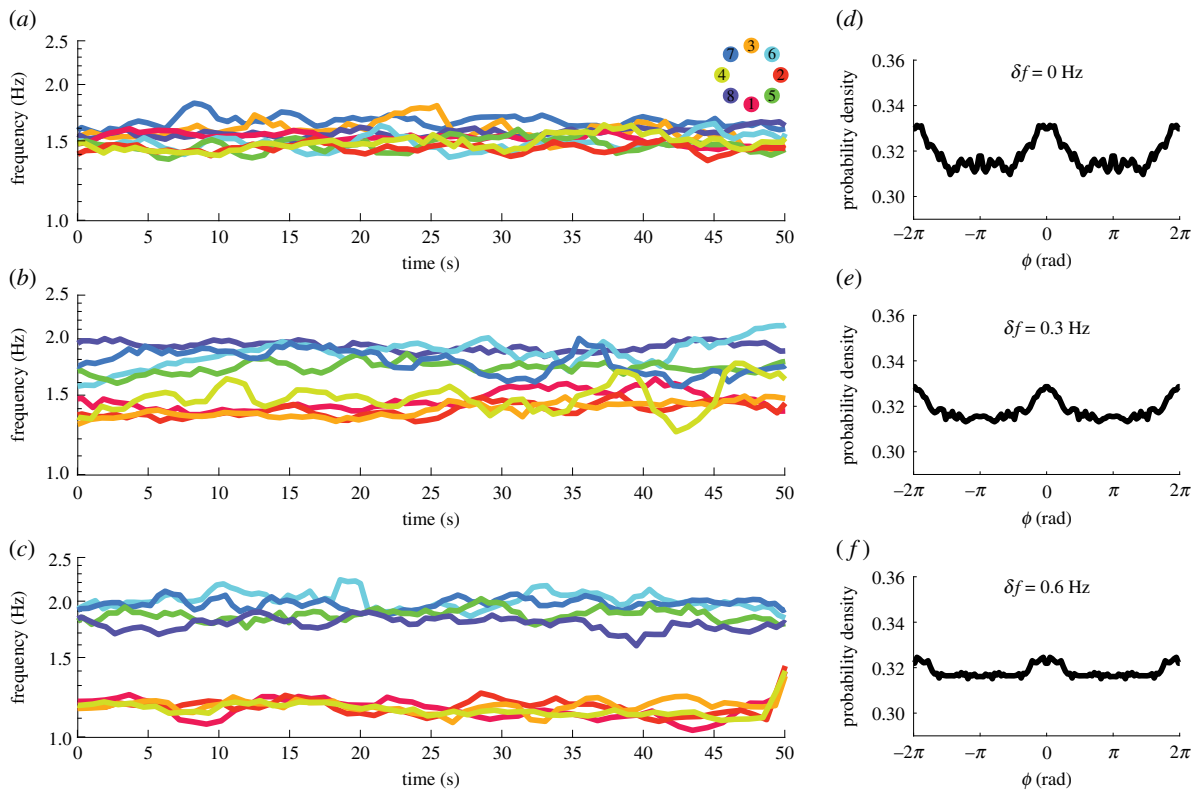
Figure 2. Social coordination behaviour observed in the Human Firefly experiment in terms of frequency dynamics and aggregated relative phase distributions. Panels (*a–c*) show instantaneous frequency (average over four cycles) from three example trials with diversity $\delta f = 0$, 0.3, 0.6 Hz, respectively. Viewed from bottom to top, in (*c*), two frequency groups of four are apparent and isolated due to high intergroup difference (low-frequency group, warm colours, paced with metronome $f_A = 1.2$ Hz; high-frequency group, cold colours, paced with metronome $f_B = 1.8$ Hz). As the two groups get closer (*b*), more cross-talk occurred between them (note contacting trajectories especially after 30 s). Finally, when the intergroup difference is gone (*a*), one supergroup of eight formed. Panels (*d–f*) show relative phase ϕ distributions aggregated from all trials for $\delta f = 0$, 0.3, 0.6 Hz, respectively (each distribution was computed from the set of all pair-wise relative phases at all time points in all trials for a given diversity condition; histograms computed in $[0, \pi)$, plotted in $[-2\pi, 2\pi]$ to reflect the symmetry and periodicity of relative phase distributions). When diversity is low (*d*), the distribution peaks near inphase ($\phi = 0$) and antiphase ($\phi = \pi$), separated by a trough near $\pi/2$, with antiphase weaker than inphase. The two peaks are diminished as δf increases (*e,f*), but the weaker one at antiphase becomes flat first (*f*). (Online version in colour.)

nonlinearly on diversity δf, and as a result the theoretical δf^* is 0.4 Hz (figure 4*d*). This prediction can be tested in future experiments by making finer divisions between $\delta f = 0.3$ and 0.6 Hz.

In the human experiment, not only did we uncover the effect of diversity on intergroup relations, but also, non-trivially, on intragroup coordination (outside affects within, a sign of complexity). Statistically, this is shown in figure 3*b* (three bars on the left): with the presence of intergroup difference ($\delta f > 0$), intragroup coordination was reduced (red, yellow bars significantly shorter than blue bar). This is well captured by the model as shown in figure 3*d* (two-way ANOVA interaction effect, $F_{2,19194} = 3416$, $p < 0.001$; the simulated data also capture the rapid decline of intergroup coordination with increasing δf in human data, shown in figure 3*b,d*, right). In addition to capturing this statistical reduction of intragroup coordination due to intergroup difference, the model, more importantly, provides a window to the dynamical mechanism underlying such statistical phenomena. For example, comparing three simulated trials with identical intragroup properties but different levels of intergroup difference (figure 5*a–c*), we see that the presence of intergroup difference (figure 5*b,c* for $\delta f = 0.3$, 0.6 Hz) dramatically elevates metastability in the system (compare intermittently converging–diverging dynamics in figure 5*b,c* to the rather constant behaviour in figure 5*a* for

$\delta f = 0$). This suggests that the decrease of intragroup coordination in a statistical sense reflects the increase of metastability in a dynamical sense (see section 'Examples of dynamics with intergroup coupling removed' in the electronic supplementary materials for baseline dynamics when intergroup coupling is removed). Indeed, if we remove intragroup metastability from all simulations (by reducing intragroup frequency variability), they no longer capture the empirically observed statistical result (see section 'Effect of reduced intragroup variability in natural frequency' in the electronic supplementary materials).

At the interpersonal level, human subjects tended to coordinate with each other around inphase and antiphase, especially when the diversity is low ($\delta f = 0$ Hz; figure 2*d*, peaks around $\phi = 0$, π separated by a trough near $\phi = \pi/2$); and the preference for inphase and antiphase both diminishes as diversity increases ($\delta f = 0.3$, 0.6, figure 2*e,f*). Both aspects are well reproduced in simulations of the model (figure 5*d–f*). Note that these model-based distributions are overall less dispersed than the more variable human-produced distributions (figure 2*d–f*), likely due to the deterministic nature of the model (i.e. no stochastic terms). Yet as demonstrated above, a deterministic model is sufficient for capturing key empirical results at all three levels of description, i.e. coexistence of inphase and antiphase tendencies and their reduction with diversity, reduction of intragroup coordination with the
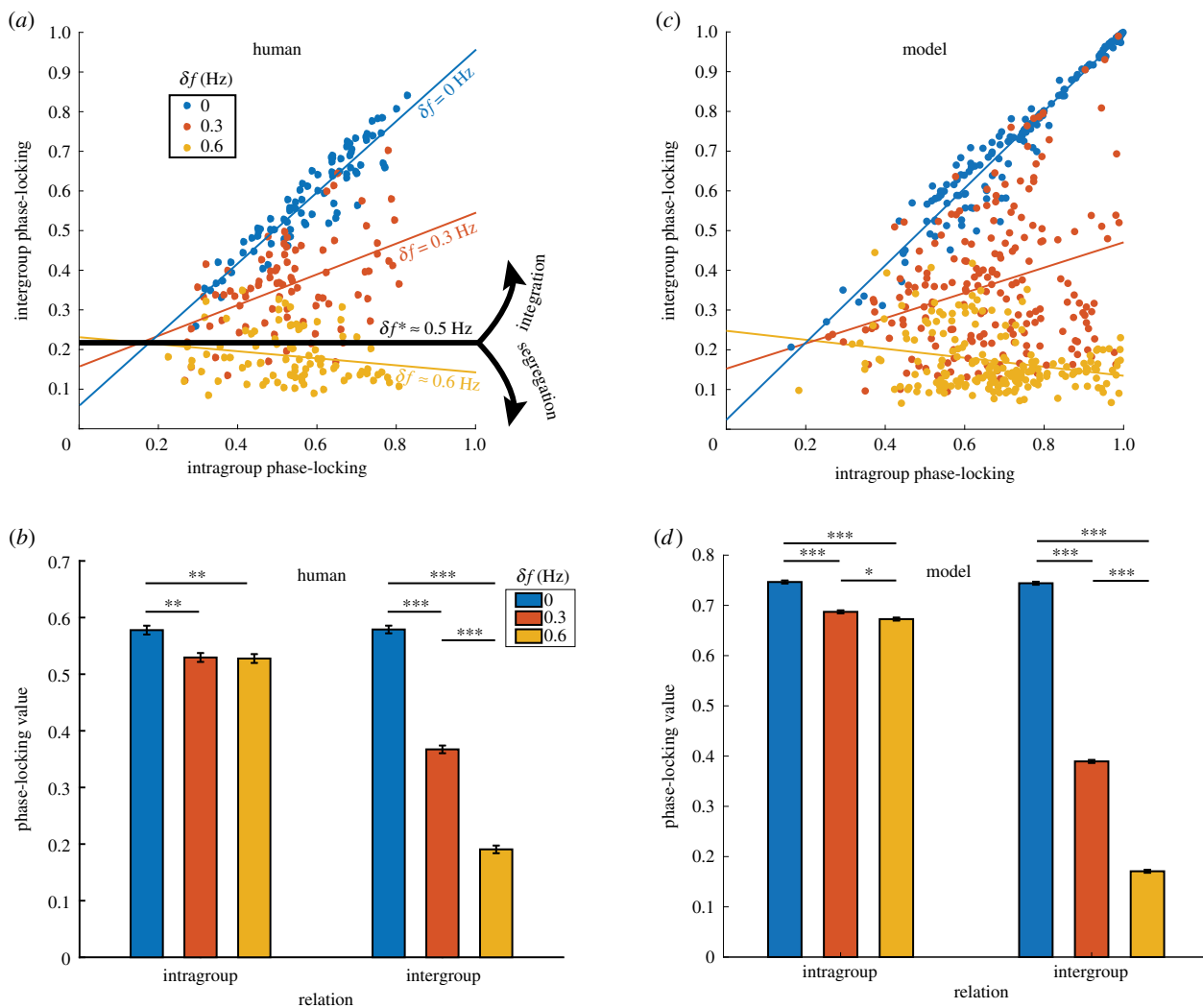
Figure 3. Comparison between human and model behaviour at intragroup and intergroup levels. (a) How intragroup coordination relates to intergroup coordination for different levels of diversity (δf, colour-coded) in the 'Human Firefly' experiment [24]. Each dot's x- and y-coordinate reflect the level of intragroup and intergroup coordination, respectively (measured by phase-locking value; see text) for a specific trial. Lines of corresponding colours are regression lines fitted for each diversity condition (slope β_1 indicates the level of integration between groups). With low and moderate diversity (blue and red), two frequency groups are integrated (positive slopes); and with high diversity (yellow), two frequency groups are segregated (negative slope). Black line (zero slope) indicates the empirically estimated critical diversity δf^*, demarcating the regimes of intergroup integration and segregation. The exact same analyses applied to the simulated data (200 trials per diversity condition) and results are shown in (c), which highly resemble their counterparts in (a). (b) A break-down of the average level of dyadic coordination as a function of diversity (colour) and whether the dyadic relation was intragroup (left) or intergroup (right). Intragroup coordination was reduced by the presence of intergroup diversity ($\delta f \neq 0$; left red, yellow bars shorter than left blue bar); intergroup coordination dropped rapidly with increasing δf (right three bars; error bars reflect standard errors). Results of the same analyses on simulated data are shown in (d), which again highly resemble those of the human data in (b). (Online version in colour.)

presence of intergroup difference, and intergroup integration~segregation at different levels of diversity. Thus, the deterministic version of the model is preferred for simplicity.

2.4. The necessity of second-order coupling

Equation (2.3) becomes the classical Kuramoto model [2] when $b = 0$. We follow the same analyses as in the previous section but now for $a = 0.154$ and $b = 0$ (see section 'Intergroup relation without second order coupling' in the electronic supplementary material on parameter choices). The relationship between intragroup and intergroup coordination (electronic supplementary material, figure S8A; $\beta_1(0 \text{ Hz}) = 0.974$, $t_{199} = 53.2$, $p < 0.001$; $\beta_1(0.3 \text{ Hz}) = 0.292$, $t_{199} = 4.52$, $p < 0.001$; $\beta_1(0.6 \text{ Hz}) = -0.011$, $t_{199} = -0.41$, $p > 0.05$) resembles the case of $b \neq 0$ ($a = b = 0.105$, figure 3c). A difference remains that for $b = 0$, $\beta_1(0.6 \text{ Hz})$ is not significantly less than zero ($p = 0.68$;

electronic supplementary material, figure S8A yellow). The average level of intragroup and intergroup coordination also varies with diversity in the same way as the case of $b \neq 0$ (electronic supplementary material, figure S8b for $b = 0$, interaction effect $F_{2,19194} = 3737$, $p < 0.001$, compared to figure 3d for $b \neq 0$). In short, group-level statistical features can be mostly preserved without second-order coupling (i.e. $b = 0$).

However, this is no longer the case when it comes to interpersonal relations. The distributions of dyadic relative phases are shown in figure 5g–i. Without second-order coupling, the model does not show a preference for antiphase in any of the three diversity conditions, thereby missing an important feature of human social coordination (for additional comparisons between human and model behaviour, see section 'Additional analyses on the coexistence of inphase and antiphase preference' in the electronic supplementary materials). Analytically, we find that the coupling ratio $\kappa =$
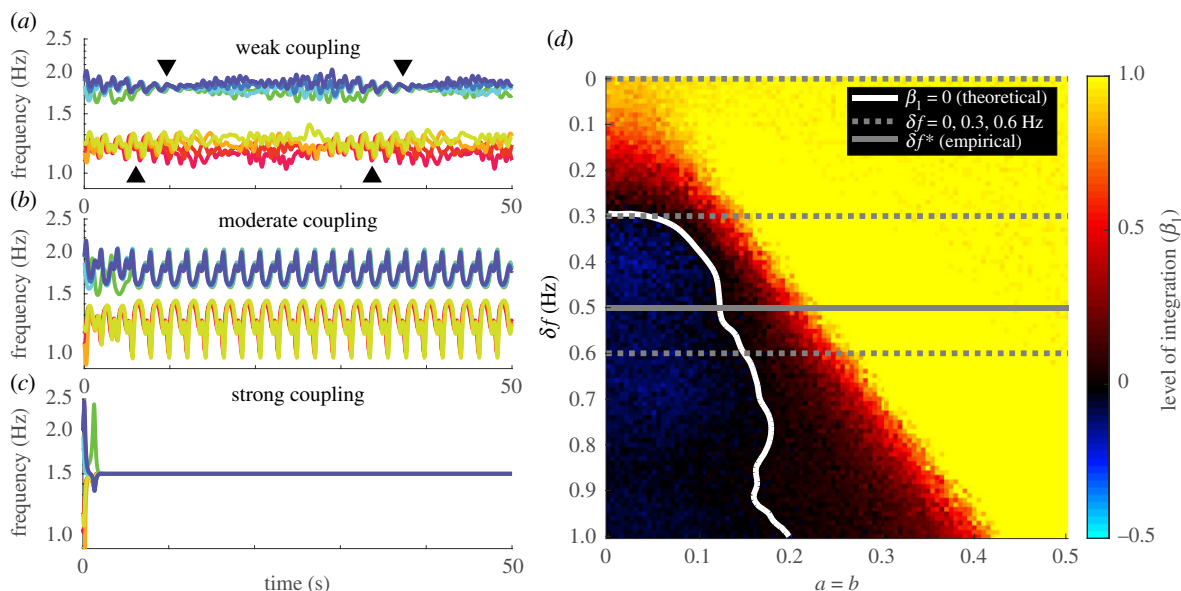
Figure 4. Simulated coordination dynamics changes qualitatively and quantitatively with coupling strength and frequency diversity. (a–c) Frequency dynamics of three simulated trials, with increasing coupling strength ($a = b = 0.1$, 0.2, 0.4, respectively) and all other parameters identical (members of the slower group, in warm colours, spread evenly within the interval 1.2 ± 0.08 Hz, similarly for members of the faster group, in cold colours, in the interval 1.8 ± 0.08 Hz; initial phases are random across oscillators but the same across trials). When the coupling is too strong (c), all oscillators lock to the same steady frequency. When the coupling is moderate (b), oscillators split into two frequency groups, phase-locked within themselves, interacting metastably with each other (dwell when trajectories are close, escape when trajectories are far apart). When the coupling is weak (a), intragroup coordination also becomes metastable seen as episodes of convergence (black triangles) and divergence. (d) Level of intergroup integration quantitatively (β_1, colour of each pixel) for each combination of frequency diversity δf and coupling strength $a = b$. White curve indicates the critical boundary between segregation (blue area on the left, $\beta_1 < 0$, $\min \beta_1 = -0.2$) and integration (red and yellow area on the right, $\beta_1 > 0$). Within the regime of integration, the yellow area indicates complete integration ($\beta_1 \approx 1$) where there is a high level of phase locking, and the red area indicates partial integration ($0 < \beta_1 \ll 1$) suggesting metastability. Dashed grey lines label δf's that appeared in the human experiment. Solid grey line labels the empirically estimated critical diversity. (Online version in colour.)

$2b/a$ determines whether antiphase is preferred (for the simple case of identical oscillators, see section 'Multistability of the present model' in the electronic supplementary materials). A critical coupling ratio $\kappa_c = 1$ demarcates the regimes of monostability (only all-inphase is stable for $\kappa < 1$) and multistability (any combination of inphase and antiphase is stable for $\kappa > 1$). This critical ratio (for equation (2.3)) is identical to the critical coupling of the HKB model [29], where the transition between monostability (inphase) and multistability (inphase and antiphase) occurs (equation (2.2); parameters in the two equations map to each other by $a = \tilde{a}/2$ and $b = \tilde{b}$). This shows how equation (2.3) is a natural N-dimensional generalization of the extended HKB model, in terms of multistability and order-to-order transitions.

2.5. The effect of non-uniform coupling

So far, our model has captured very well experimental observations with the simple assumption of uniform coupling. However, loosening this assumption is necessary for understanding detailed dynamics. Here is an example from [24] (figure 6a), where coordination among three agents (1, 3 and 4, labels of locations on LED arrays) is visualized as the dynamics of two relative phases (ϕ_{13} red, ϕ_{34} yellow). Agents 3 and 4 coordinated inphase persistently (10–40 s yellow trajectory flat at $\phi_{34} \approx 0$), while agents 3 and 1 coordinated intermittently every time they passed by inphase (red trajectory ϕ_{13} became flat, i.e. dwells, near inphase around 10, 20 and 35 s). Curiously, every dwell in ϕ_{13} (red) was accompanied by a little bump in ϕ_{34}, suggesting ϕ_{34} was periodically influenced by ϕ_{13}. In the framework of our

model, we can approximate the dynamics of ϕ_{34} from equation (2.1) by assuming $\phi_{34} = 0$ (thus $\phi_{13} = \phi_{14}$),

$$\dot{\phi}_{34} = f(\phi_{34}) + \underbrace{(a_{31} - a_{41})\sin\phi_{13} + (b_{31} - b_{41})\sin 2\phi_{13}}_{=:K(\phi_{13})}, \quad (2.4)$$

where $f(\phi_{34})$ is the influence of ϕ_{34} on itself, $K(\phi_{13})$ the influence of ϕ_{13} on ϕ_{34}. From $K(\phi_{13})$, we see that ϕ_{13} has no influence on ϕ_{34} if the coupling is completely uniform (i.e. $K(\phi_{13}) \equiv 0$ if $a_{31} = a_{41}$ and $b_{31} = b_{41}$), making it impossible to capture the empirical observation (red relation influencing yellow relation, figure 6a). To break the symmetry between agent 3 and 4, we 'upgrade' equation (2.3) to the system

$$\dot{\varphi}_i = \omega_i - a_i \sum_{j=1}^{N} \sin\phi_{ij} - b_i \sum_{j=1}^{N} \sin 2\phi_{ij}, \quad (2.5)$$

where each oscillator can have its own coupling style (oscillator specific coupling strength a_i and b_i). In the present case, we are interested in what happens when $a_3 \neq a_4$ for $i \in \{1, 3, 4\}$. Two simulated trials are shown in figure 6b and c with non-uniform versus uniform coupling (same initial conditions and natural frequencies across trials, estimated from the human data). The bumps in ϕ_{34}, accompanying dwells in ϕ_{13}, are reproduced when $a_3 \gg a_4$ (figure 6b) but not when $a_3 = a_4$ (figure 6c; see section 'Additional triadic dynamics' in the electronic supplementary materials for more analyses). This example shows that to understand interesting dynamic patterns in specific trials, non-uniform coupling strength is important.
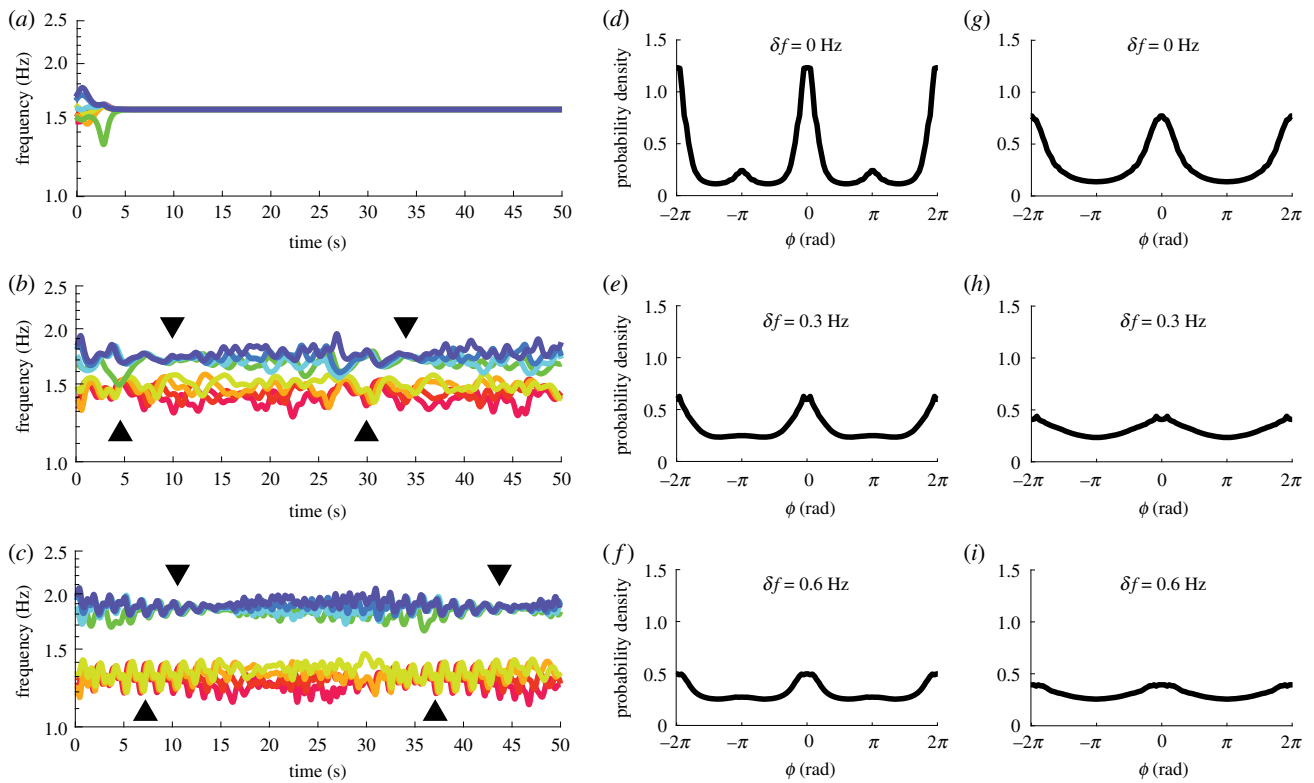
Figure 5. Model simulations of frequency dynamics and aggregated relative phase distributions. (a–c) An example of how intergroup difference may affect intragroup coordination using frequency dynamics of three simulated trials ($a = b = 0.105$; note that frequency is the time derivative of phase divided by 2π, and consequently the distance between two frequency trajectories reflects the rate of change of the corresponding relative phase, which increases and decreases intermittently during metastable coordination). These three trials share the same initial phases and intragroup frequency dispersion but different intergroup difference i.e. $\delta f = 0$, 0.3, 0.6 Hz, respectively. When intergroup differences are introduced (b,c), not only is intergroup interaction altered but intragroup coordination also loses stability and becomes metastable (within-group trajectories converge at black triangles and diverge afterwards). The timescale of metastable coordination also changes with δf, i.e. the inter-convergence interval is shorter for (b) than (c). (d–f) Relative phase distributions, aggregated over all time points in 200 trials ($a = b = 0.105$) for each diversity condition ($\delta f = 0$, 0.3, 0.6, respectively). At low diversity (d), there is a strong inphase peak and a weak antiphase peak, separated by a trough near $\pi/2$. Both peaks are diminished by increasing diversity (e,f). These features match qualitatively the human experiment. (g–i) The same distributions as (d–f) but for $a = 0.154$ and $b = 0$ (i.e. the classical Kuramoto model). There is a single peak in each distribution at inphase $\phi = 0$, and a trough at antiphase $\phi = \pi$. (Online version in colour.)

3. Discussion

The present model successfully captures key features of multiagent coordination in mid-scale ensembles at multiple levels of description [24]. Similar to the HKB model [29], second-order coupling is demanded by the experimental observation of antiphase (and associated multistability) but now in eight-person coordination; and similar to the extended HKB [37], the model captures how increasing frequency difference δf weakens inphase and antiphase patterns, leading to segregation but now between two groups instead of two persons. This cross-scale consistency of experimental observations may be explained by the scale-invariant nature of the critical coupling ratio $\kappa_c = 1$, the transition point between monostability (only an all-inphase state) and multistability (states containing any number of antiphase relations). The scale invariance suggests that experimental methods and conclusions for small-scale coordination dynamics have implications for multistability, phase transitions and metastability at larger scales, and enables a unified approach to biological coordination that meshes statistical mechanics and nonlinear dynamics.

Another generalization of the classical Kuramoto model by Hong & Strogatz [45] also allows for antiphase-containing patterns (π-state) by letting the sign of the first-order coupling

(a) be positive for some oscillators (the conformists) and negative for others (the contrarians). However, in contrast to our model, antiphase induced this way does not come with multistability, nor the associated order-to-order transitions observed in human rhythmic coordination [13,46]. The second-order coupling in our model allows each individual to be *both* a conformist *and* a contrarian but possibly to different degrees [47]. The simple addition of a second stable state may not seem like a big plus at $N = 2$ (2 stable states), but it rapidly expands the system's behavioural repertoire as the system becomes larger (2^{N-1} stable states for N oscillators; with only first-order coupling, the system always has $1^{N-1} = 1$ stable state, and therefore does not benefit from scaling up). This benefit of scale may be how micro-level multistability contributes to the functional complexity of biological systems [43,48].

Outside of the mathematical context of stability analysis, we have to recall that spontaneous social coordination is highly metastable (e.g. figure 2a) [24], captured by the model when frequency diversity is combined with weak coupling (e.g. figure 4a, in contrast to b,c under stronger coupling). Individuals did not become phase-locked in the long term, but coordinated temporarily when passing by a preferred state (inphase and antiphase) [14,43] (e.g. red trajectory in figure 6a). For $N > 2$, an ensemble can visit different spatial
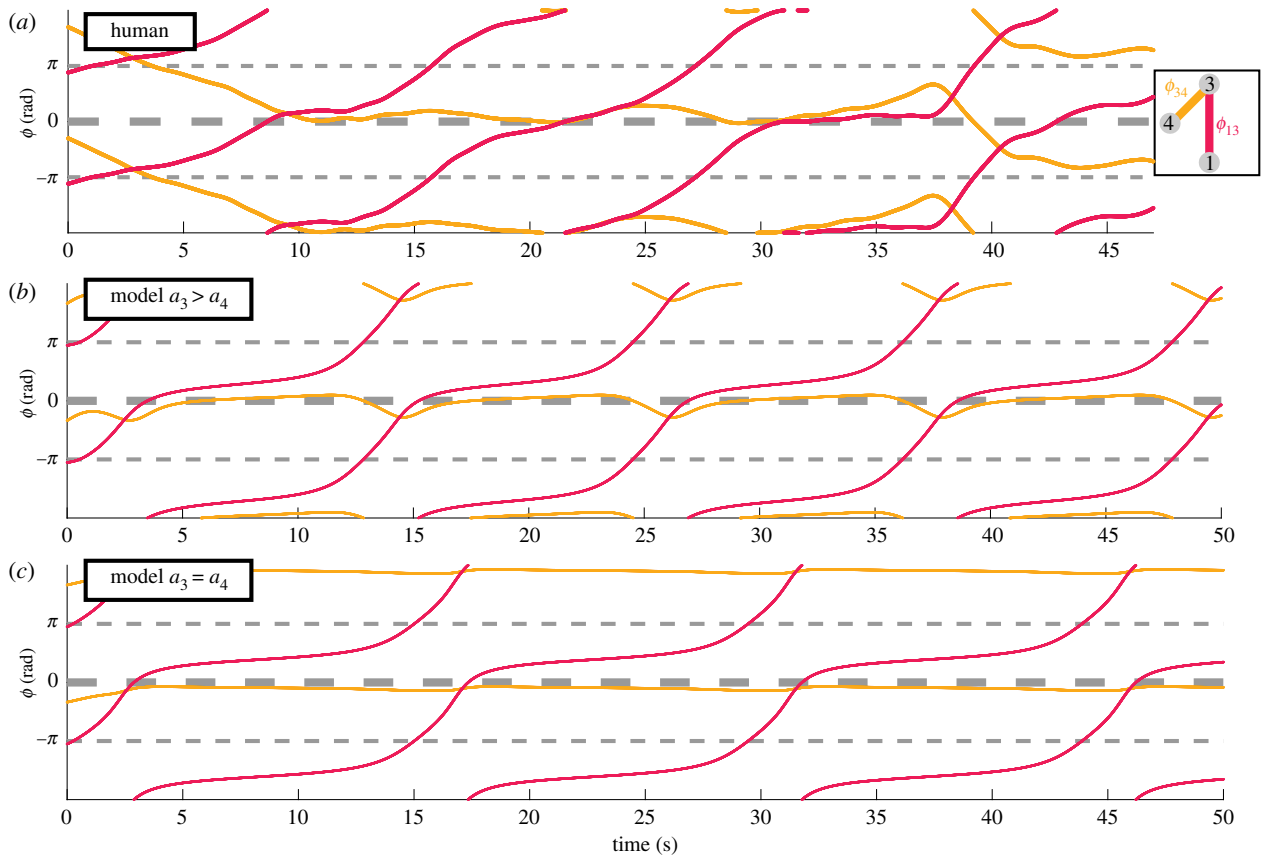
Figure 6. Model with non-uniform coupling captures detailed relative phase dynamics observed in human social coordination. (a) Experimental observation of the coordination dynamics between three persons (agent 1, 3, 4, spatially situated as in legend) in terms of two relative phases (ϕ_{13}, ϕ_{34}; y-coordinates) as a function of time (x-coordinates). ϕ_{34} (yellow) persisted at inphase for a long time (10–37 s trajectory flattened near $\phi = 0$) before switching to antiphase (40 s; inphase and antiphase are labelled with thick and thin dashed lines, respectively, throughout this figure). ϕ_{13} (red) dwelt at inphase intermittently (flattening of trajectory around 10, 20, and 35 s). Three bumps appeared in ϕ_{34} during its long dwell at inphase (near 15, 25, 37 s), which followed the dwells in ϕ_{13}, indicating a possible influence of ϕ_{13} on ϕ_{34}. (b,c) Two simulated trials with identical initial conditions and natural frequencies, estimated from the human data. In (b), agent 3 is more 'social' than agent 4 ($a_3 > a_4$). More precisely, agent 3 has a much stronger coupling ($a_3 = 1$) than all others ($a_1 = a_4 = b_1 = b_3 = b_4 = 0.105$, as in previous sections). The recurring bumps in ϕ_{34} are nicely reproduced. In (c), agents 3 and 4 are equally 'social' ($a_3 = a_4 = 0.5525$, keeping the same average as in (b)). ϕ_{34} is virtually flat throughout the trial. (Online version in colour.)

organizations sequentially (see examples in [24]), forming patterns that extend in both space and time (electronic supplementary material, figure S4 for intragroup patterns), which further expands the repertoire of coordinative behaviour (see section 'A note on metastability' in the electronic supplementary materials). By allowing complex patterns to be elaborated over time, metastability makes a viable mechanism for encoding complex information as real-world complex living systems do (e.g. the brain) [13,14,22,49–52]. By contrast, highly coherent patterns like collective synchronization can be less functional and even pathological [53,54]. Our results call for more attention to these not-quite coherent but empirically relevant patterns of coordination.

Besides the multistability or multi-clustering in micro patterns (a general feature endowed by higher-order coupling, e.g. [55–57]), existing mathematical studies suggest that the presence of second-order coupling should also manifest at the macro level in large-scale coordination. Naturally, second-order coupling induces multistability of the order parameter in the thermodynamic limit [58–61]. It also alters the critical scaling of macroscopic order (see [41] for a summary), i.e. for coupling strength $K > K_c$ near K_c, the order parameter $\|H\|$ (norm of the order function [62]) is proportional to $(K - K_c)^\beta$, with $\beta = 1/2$ for the classical Kuramoto model and $\beta = 1$ when second-order coupling is

added [63,64]. For complex biological systems like the brain which appears to operate near criticality [65], these two types of scaling behaviour may have very different functional implications. When modelling empirical data of biological coordination, one may want to have a closer examination or re-examination of the data for multistability and critical scaling of the order parameter, especially if finer level details are not available.

Key experimental observations are captured by our model under the assumptions of uniform coupling (everyone coordinates with others in the same way) and constant natural frequency, but these assumptions may be loosened to reflect detailed dynamics. For example, introducing individual differences in coupling style (equation (2.5)) gives more room to explain how one metastable phase relation may exert strong influence on another (figure 6a). Long timescale dynamics observed in the experiment (see section 'Additional triadic dynamics' in the electronic supplementary materials) may also be explained by frequency adaptation, which has been observed in dyadic social coordination [66]. A systematic study of the consequences of asymmetric coupling and frequency adaptation on coordination among multiple agents seems worthy of further experimental and theoretical exploration.

To conclude, we proposed a model that captured key features of human social coordination in mid-sized ensembles

[24], and at the same time connects empirically validated large-scale and small-scale models of biological coordination. The model provides mechanistic explanations of the statistics and dynamics already observed, as well as a road map for future empirical exploration. As an experimental–theoretical platform for understanding biological coordination, the value of the middle scale should not be underestimated, nor the importance of examining coordination phenomena at multiple levels of description.

4. Material and methods

4.1. Methods of the human experiment

A complete description of the methods of the 'Human Firefly' experiment can be found in [24]. Here we provide as many details as necessary for understanding the present paper. A total of 120 subjects participated in the experiment, making up 15 independent ensembles of eight people. The protocol was approved by Florida Atlantic University Institutional Review Board and is in agreement with the Declaration of Helsinki. Informed consent was obtained from all participants prior to the experiment.

For an ensemble of eight people, each subject was equipped with a touchpad that recorded his/her tapping behaviour as a series of zeros and ones at 250 Hz (1 = touch, 0 = detach; green rectangles in figure 1), and an array of eight LEDs arranged in a ring (yellow in figure 1), each of which flashed when a particular subject tapped. For each trial, subjects were first paced with metronomes for 10 s, later interacting with each other for 50 s (instructed to maintain metronome frequency while looking at others' taps as flashes of the LEDs). Between the pacing and interaction period, there was a 3 s transient, during which subjects tapped by themselves. Participants were instructed to match their own tapping frequency to the metronome frequency during the 10 s pacing period, and remain tapping at that frequency throughout the rest of the trial even after the metronome disappeared.

During pacing, four subjects received the same metronome (same frequency, random initial phase), and the other four another metronome. The metronome assignments created two frequency groups (say, group A and B) with intergroup difference $\delta f = |f_A - f_B| = 0$, 0.3 or 0.6 Hz (same average $(f_A + f_B)/2 = 1.5$ Hz). This gives rise to three conditions: (1) 1.5 Hz versus 1.5 Hz, (2) 1.65 Hz versus 1.35 Hz, and (3) 1.8 Hz versus 1.2 Hz. Each ensemble completed six trials per condition (a total of 18 trials in random order). From a single subject's perspective, the LED array looks like the legend of figure 2a (all LEDs emit white light; colour-coding only for labelling locations): a subject always saw his/her own taps as the flashes of LED 1, members of his/her own frequency group LED 2–4, and members of the other group LED 5–8 (members from two groups were interleaved to preserve spatial symmetry).

From the tapping data (rectangular waves of zeros and ones), we obtained the onset of each tap, from which we calculated instantaneous frequency and phase. Instantaneous frequency is the reciprocal of the interval between two consecutive taps. Phase (φ) is calculated by assigning the onset of the nth tap phase $2\pi(n-1)$, then interpolating the phase between onsets with a cubic spline. The relative phase between the ith and jth subject at time t is $\phi_{ij}(t) = \varphi_i(t) - \varphi_j(t)$.

4.2. Estimating the distribution of natural frequencies

Human subjects have variable capability to match the metronome frequency and maintain it, which in turn affects how they coordinate. To reflect this kind of variability in the

simulations, the oscillators' natural frequencies were drawn from a probability distribution around the 'metronome frequency' (central frequencies f_A and f_B for groups A and B). To estimate this distribution from human data, we first approximated the 'natural frequency' of each subject in each trial with the average tapping frequency during the transient between pacing and interaction periods (see Methods of the human experiment), and subtracted from it the metronome frequency (see blue histogram in electronic supplementary material, figure S3 from the 'Human Firefly' experiment [24]). We then estimated the distribution non-parametrically, with a *kernel density estimator* in the form of

$$\hat{P}(x) = \frac{1}{nh}\sum_{i=1}^{n} K\left(\frac{x - x_i}{h}\right), \tag{4.1}$$

where the *Kernel Smoothing Function* is Normal, $K(y) = \left(1/\sqrt{2\pi}\right)e^{-y^2/2}$. Here $n = 2072$ (259 trials × 8 subjects) from the experiment. We choose the bandwidth $h = 0.0219$, which is optimal for a normal density function according to [67],

$$h = \left(\frac{4}{3n}\right)^{1/5}\sigma, \tag{4.2}$$

where σ is the measure of dispersion, estimated by

$$\tilde{\sigma} = \frac{\text{median}\{|y_i - \text{median}\{y_i\}|\}}{0.6745}, \tag{4.3}$$

where y_i's are samples [68]. The result of the estimation is shown in electronic supplementary material, figure S3 (red curve).

4.3. Phase-locking value and level of integration

The (short-windowed) phase-locking value (PLV) between two oscillators (say x and y) during a trial is defined as

$$\text{PLV}_{xy} = \frac{1}{W}\sum_{w=1}^{W}\frac{1}{M}\left|\sum_{m=1}^{M}\exp\left(\text{i}\phi_{xy}[(w-1)M + m]\right)\right|, \tag{4.4}$$

where $\phi_{xy} = \varphi_x - \varphi_y$, W is the number of windows which each ϕ trajectory is split into, and M is number of samples in each window (in the present study, $W = 16$ and $M = 750$, same as [24]).

Intragroup PLV ($\text{PLV}_{\text{intra}}$) is defined as

$$\text{PLV}_{\text{intra}} = \left(\binom{|A|}{2} + \binom{|B|}{2}\right)^{-1}\left(\sum_{x,y\in A}\text{PLV}_{xy} + \sum_{x,y\in B}\text{PLV}_{xy}\right), \tag{4.5}$$

where A and B are two frequency groups of four oscillators, corresponding to the design of the 'Human Firefly' experiment [24], $A = \{1, 2, 3, 4\}$, $B = \{5, 6, 7, 8\}$ and $|A| = |B| = 4$.

Intergroup PLV ($\text{PLV}_{\text{inter}}$) is defined as

$$\text{PLV}_{\text{inter}} = \frac{1}{|A||B|}\sum_{x\in A, y\in B}\text{PLV}_{xy}. \tag{4.6}$$

In both the human and simulated data, comparisons of $\text{PLV}_{\text{intra}}$ and $\text{PLV}_{\text{inter}}$ for different levels of δf were done using two-way ANOVA with Type III sums of squares, and Tukey honest significant difference tests for post-hoc comparisons (shown in figure 3b,d).

The level of integration between two frequency groups is defined based on the relationship between intragroup coordination (measured by $\text{PLV}_{\text{intra}}$) and intergroup coordination (measured by $\text{PLV}_{\text{inter}}$). The groups are said to be *integrated* if intragroup coordination is positively related to intergroup coordination, and *segregated* if negatively related. Quantitatively, for each combination of intergroup difference δf and coupling strength a (assuming $a = b$ for our model, assuming $b = 0$ for the

classical Kuramoto model), we use linear regression

$$\mathrm{PLV}_{\mathrm{inter},k}^{(\delta f, a)} = \beta_0^{(\delta f, a)} + \beta_1^{(\delta f, a)}\, \mathrm{PLV}_{\mathrm{intra},k}^{(\delta f, a)} + \mathrm{error}_k^{(\delta f, a)}, \qquad (4.7)$$

where $\mathrm{PLV}_{\cdot,k}^{(\delta f, a)}$ is the inter/intra-group PLV for the kth trial simulated with the parameter pair $(\delta f, a)$, and the slope of the regression line $\beta_1^{(\delta f, a)}$ is defined as the measure of the *level of integration* between two frequency groups. If $\beta_1 > 0$, the groups may be said to be integrated; if $\beta_1 < 0$, segregated. The set $\{(\delta f, a)|\beta_1^{(\delta f, a)} = 0\}$ is the *critical boundary* between the domains of intergroup integration and segregation. Theoretical analyses (section 'Choosing the appropriate coupling strength' in the electronic supplementary materials) show that this measure is meaningful (i.e. reflecting qualitative differences between dynamics; figure 4a–c).

4.4. Method of simulation

All simulations were done using the Runge–Kutta 4th-order integration scheme, with a fixed time step $\Delta t = 0.004$ for duration $T = 50$ (matching the sampling interval and the duration of interaction period of the human experiment [24]; second may be used as unit), i.e. for system $\dot{X} = f(X)$, with initial condition $X(0) = X_0$, the $(n+1)$th sample of the numeric solution can be solved recursively

$$X[n+1] = X[n] + \frac{1}{6}(k_1 + 2k_2 + 2k_3 + k_4), \qquad (4.8)$$

where

$$k_1 = \Delta t f(X[n]), \qquad (4.9)$$

$$k_2 = \Delta t f\left(X[n] + \frac{k_1}{2}\right), \qquad (4.10)$$

$$k_3 = \Delta t f\left(X[n] + \frac{k_2}{2}\right) \qquad (4.11)$$

and

$$k_4 = \Delta t f(X[n] + k_3). \qquad (4.12)$$

The solver was implemented in CUDA C++, ran on a NVIDIA graphics processing unit, solving every 200 trials in parallel for each parameter pair $(\delta f, a)$. For each trial, initial phases (of eight oscillators) were drawn randomly from a uniform distribution between 0 and 2π, and natural frequencies from distributions defined by equation (4.2) (reflecting the design of and variability observed in the human experiment [24]). Here 200 trials are used per condition, greater than that of the human experiment (see [24] and section 'Design of the human experiment' in the electronic supplementary materials for details) to obtain a more accurate estimate of the mean.

References

1. Winfree AT. 1987 *The timing of biological clocks*. New York, NY: Scientific American Books.

2. Kuramoto Y. 1984 *Chemical oscillations, waves, and turbulence,* vol. 19 of Springer Series in Synergetics. Berlin, Germany: Springer.

3. Glass L. 2001 Synchronization and rhythmic processes in physiology. *Nature* **410**, 277–284. (doi:10.1038/35065745)

4. Nakagaki T, Yamada H, Ueda T. 2000 Interaction between cell shape and contraction pattern in the *Physarum plasmodium*. *Biophys. Chem.* **84**, 195–204. (doi:10.1016/S0301-4622(00)00108-3)

5. Kobayashi R, Tero A, Nakagaki T. 2006 Mathematical model for rhythmic protoplasmic movement in the true slime mold. *J. Math. Biol.* **53**, 273–286. (doi:10.1007/s00285-006-0007-0)

6. Buck J, Buck E. 1966 Biology of synchronous flashing of fireflies. *Nature* **211**, 562–564. (doi:10.1038/211562a0)

7. Mirollo RE, Strogatz SH. 1990 Synchronization of pulse-coupled biological oscillators. *SIAM J. Appl. Math.* **50**, 1645–1662. (doi:10.1137/0150098)

8. Néda Z, Ravasz E, Brechet Y, Vicsek T, Barabási AL. 2000 The sound of many hands clapping. *Nature* **403**, 849–850. (doi:10.1038/35002660)

9. Richardson MJ, Marsh KL, Isenhower RW, Goodman JRL, Schmidt RCC. 2007 Rocking together: dynamics of intentional and unintentional interpersonal coordination. *Hum. Mov. Sci.* **26**, 867–891. (doi:10.1016/j.humov.2007.07.002)

10. Grillner S. 1985 Neurobiological bases of rhythmic motor acts in vertebrates. *Science* **228**, 143–149. (doi:10.1126/science.3975635)

11. Marder E, Calabrese RL. 1996 Principles of rhythmic motor pattern generation. *Physiol. Rev.* **76**, 687–717. (doi:10.1152/physrev.1996.76.3.687)

12. Bressler SL, Kelso JAS. 2001 Cortical coordination dynamics and cognition. *Trends Cogn. Sci.* **5**, 26–36. (doi:10.1016/S1364-6613(00)01564-3)

13. Kelso JAS. 1995 *Dynamic patterns: the self-organization of brain and behavior*. Cambridge, MA: The MIT Press.

14. Tognoli E, Kelso JAS. 2014 The metastable brain. *Neuron* **81**, 35–48. (doi:10.1016/j.neuron.2013.12.022)

15. Winfree AT. 2001 *The geometry of biological time*, vol. 12 of interdisciplinary applied mathematics. New York, NY: Springer.

16. Schöner G, Kelso JAS. 1988 Dynamic pattern generation in behavioral and neural systems. *Science* **239**, 1513–1520. (doi:10.1126/science.3281253)

17. Rand RH, Cohen AH, Holmes PJ. 1988 Systems of coupled oscillators as models of central pattern generators. In *Neural control of rhythmic movements in vertebrates* (ed. AH Cohen), pp. 333–367. New York, NY: John Wiley & Sons.

18. Kopell N, Ermentrout GB. 1988 Coupled oscillators and the design of central pattern generators. *Math. Biosci.* **90**, 87–109. (doi:10.1016/0025-5564(88)90059-4)

19. Jeka JJ, Kelso JAS, Kiemel T. 1993 Pattern switching in human multilimb coordination dynamics. *Bull. Math. Biol.* **55**, 829–845. (doi:10.1007/BF02460675)

20. Yokoyama K, Yamamoto Y. 2011 Three people can synchronize as coupled oscillators during sports activities. *PLoS Comput. Biol.* **7**, e1002181. (doi:10.1371/journal.pcbi.1002181)

21. Acebrón JA, Bonilla LL, Pérez Vicente CJ, Ritort F, Spigler R. 2005 The Kuramoto model: a simple paradigm for synchronization phenomena. *Rev. Mod. Phys.* **77**, 137–185. (doi:10.1103/RevModPhys.77.137)

22. Breakspear M, Heitmann S, Daffertshofer A. 2010 Generative models of cortical oscillations: neurobiological implications of the Kuramoto model. *Front. Hum. Neurosci.* **4**, 1–14. (doi:10.3389/fnhum.2010.00190)

23. Castellano C, Fortunato S, Loreto V. 2009 Statistical physics of social dynamics. *Rev. Mod. Phys.* **81**, 591–646. (doi:10.1103/RevModPhys.81.591)

24. Zhang M, Kelso JAS, Tognoli E. 2018 Critical diversity: divided or united states of social coordination. *PLoS ONE* **13**, e0193843. (doi:10.1371/journal.pone.0193843)

25. Schöner G, Jiang WY, Kelso JAS. 1990 A synergetic theory of quadrupedal gaits and gait transitions. *J. Theoret. Biol.* **142**, 359–391. (doi:10.1016/S0022-5193(05)80558-2)

26. Collins JJ, Stewart I. 1993 Coupled nonlinear oscillators and the symmetries of animal gaits. *J. Nonlinear Sci.* **3**, 349–392. (doi:10.1007/BF02429870)

27. Golubitsky M, Stewart I, Buono PLL, Collins JJ. 1999 Symmetry in locomotor central pattern generators and animal gaits. *Nature* **401**, 693–695. (doi:10.1038/44416)

28. Kelso JAS. 1984 Phase transitions and critical behaviour in human bimanual coordination. *Amer. J. Physiol. Regul. Integr. Comp. Physiol.* **246**, R1000–R1004. (doi:10.1152/ajpregu.1984.246.6.r1000)

29. Haken H, Kelso JAS, Bunz H. 1985 A theoretical model of phase transitions in human hand movements. *Biol. Cybern* **51**, 347–356. (doi:10.1007/BF00336922)

30. Marder E, Bucher D. 2001 Central pattern generators and the control of rhythmic movements. *Curr. Biol.* **11**, R986–R996. (doi:10.1016/S0960-9822(01)00581-4)

31. Tognoli E, Lagarde J, DeGuzman GC, Kelso JAS. 2007 The phi complex as a neuromarker of human social coordination. *Proc. Natl Acad. Sci. USA* **104**, 8190–8195. (doi:10.1073/pnas.0611453104)

32. Schmidt RC, Richardson MJ. 2008 Dynamics of interpersonal coordination. In *Coordination: neural, behavioral and social dynamics*, vol. 2008 (eds A Fuchs, VK Jirsa), pp. 281–308. Berlin, Germany: Springer.

33. Lagarde J, Peham C, Licka T, Kelso JAS. 2005 Coordination dynamics of the horse–rider system. *J. Mot. Behav.* **37**, 418–424. (doi:10.3200/JMBR.37.6.418-424)

34. Kelso JAS, de Guzman GC, Reveley C, Tognoli E. 2009 Virtual partner interaction (VPI): exploring novel behaviors via coordination dynamics. *PLoS ONE* **4**, e5749. (doi:10.1371/journal.pone.0005749)

35. Dumas G, de Guzman GC, Tognoli E, Kelso JAS. 2014 The human dynamic clamp as a paradigm for social interaction. *Proc. Natl Acad. Sci. USA* **111**, E3726–E3734. (doi:10.1073/pnas.1407486111)

36. Hoyt DF, Taylor CR. 1981 Gait and the energetics of locomotion in horses. *Nature* **292**, 239–240. (doi:10.1038/292239a0)

37. Kelso JAS, Del Colle JD, Schöner G. 1990 Action-perception as a pattern formation process. In *Attention and performance 13: motor representation and control*, vol. 45 (ed. M Jeannerod), pp. 139–169. Hillsdale, NJ: Lawrence Erlbaum Associates, Inc.

38. Fuchs A, Jirsa VK, Haken H, Kelso JAS. 1996 Extending the HKB model of coordinated movement to oscillators with different eigenfrequencies. *Biol. Cybern* **74**, 21–30. (doi:10.1007/BF00199134)

39. Néda Z, Ravasz E, Vicsek T, Brechet Y, Barabási ALL. 2000 Physics of the rhythmic applause. *Phys. Rev. E Stat. Phys. Plasmas Fluids Related Interdiscip. Top.* **61**, 6987–6992. (doi:10.1103/physreve.61.6987)

40. Leonard NE, Shen T, Nabet B, Scardovi L, Couzin ID, Levin Sa. 2012 Decision versus compromise for animal groups in motion. *Proc. Natl Acad. Sci. USA* **109**, 227–232. (doi:10.1073/pnas.1118318108)

41. Strogatz SH. 2000 From Kuramoto to Crawford: exploring the onset of synchronization in populations of coupled oscillators. *Phys. D Nonlinear Phenom.* **143**, 1–20. (doi:10.1016/S0167-2789(00)00094-4)

42. Acebrón JA, Bonilla LL, De Leo S, Spigler R. 1998 Breaking the symmetry in bimodal frequency distributions of globally coupled oscillators. *Phys. Rev. E* **57**, 5287–5290. (doi:10.1103/PhysRevE.57.5287)

43. Kelso JAS. 2012 Multistability and metastability: understanding dynamic coordination in the brain. *Phil. Trans. R. Soc. B* **367**, 906–918. (doi:10.1098/rstb.2011.0351)

44. Schmidt RC, Turvey MT. 1994 Phase-entrainment dynamics of visually coupled rhythmic movements. *Biol. Cybern* **70**, 369–376. (doi:10.1007/BF00200334)

45. Hong H, Strogatz SH. 2011 Kuramoto model of coupled oscillators with positive and negative coupling parameters: an example of conformist and contrarian oscillators. *Phys. Rev. Lett.* **106**, 054102. (doi:10.1103/PhysRevLett.106.054102)

46. Fuchs A, Kelso JAS. 1994 A theoretical note on models of interlimb coordination. *J. Exp. Psychol. Hum. Percept. Perform.* **20**, 1088–1097.

47. Kelso JAS, Engstrom DA. 2006 *The complementary nature*. Cambridge, MA: The MIT Press.

48. Laurent M, Kellershohn N. 1999 Multistability: a major means of differentiation and evolution in biological systems. *Trends Biochem. Sci.* **24**, 418–422. (doi:10.1016/S0968-0004(99)01473-5)

49. Friston KJ. 1997 Transients, metastability, and neuronal dynamics. *NeuroImage* **5**, 164–171. (doi:10.1006/nimg.1997.0259)

50. Tognoli E, Kelso JAS. 2014 Enlarging the scope: grasping brain complexity. *Front. Syst. Neurosci.* **8**, 122. (doi:10.3389/fnsys.2014.00122)

51. Ashwin P, Orosz G, Wordsworth J, Townley S. 2007 Dynamics on networks of cluster states for globally coupled phase oscillators. *SIAM J. Appl. Dyn. Syst.* **6**, 728–758. (doi:10.1137/070683969)

52. Rabinovich MI, Huerta R, Varona P, Afraimovich VS. 2008 Transient cognitive dynamics, metastability, and decision making. *PLoS Comput. Biol.* **4**, e1000072. (doi:10.1371/journal.pcbi.1000072)

53. Jirsa VK, Stacey WC, Quilichini PP, Ivanov AI, Bernard C. 2014 On the nature of seizure dynamics. *Brain* **137**, 2210–2230. (doi:10.1093/brain/awu133)

54. Tang E *et al.* 2017 Developmental increases in white matter network controllability support a growing diversity of brain dynamics. *Nat. Commun.* **8**, 1252. (doi:10.1038/s41467-017-01254-4)

55. Okuda K. 1993 Variety and generality of clustering in globally coupled oscillators. *Physica D: Nonlinear Phenom.* **63**, 424–436. (doi:10.1016/0167-2789(93)90121-G)

56. Hansel D, Mato G. 1993 Patterns of synchrony in a heterogeneous Hodgkin–Huxley neural network with weak coupling. *Phys. A Stat. Mech. Appl.* **200**, 662–669. (doi:10.1016/0378-4371(93)90573-M)

57. Hansel D, Mato G, Meunier C. 1993 Clustering and slow switching in globally coupled phase oscillators. *Phys. Rev. E* **48**, 3470–3477. (doi:10.1103/PhysRevE.48.3470)

58. Komarov M, Pikovsky A. 2013 Multiplicity of singular synchronous states in the Kuramoto model of coupled oscillators. *Phys. Rev. Lett.* **111**, 204101. (doi:10.1103/PhysRevLett.111.204101)

59. Komarov M, Pikovsky A. 2014 The Kuramoto model of coupled oscillators with a bi-harmonic coupling function. *Phys. D Nonlinear Phenom.* **289**, 18–31. (doi:10.1016/j.physd.2014.09.002)

60. Vlasov V, Komarov M, Pikovsky A. 2015 Synchronization transitions in ensembles of noisy oscillators with bi-harmonic coupling. *J. Phys. A: Math. Theor.* **48**, 105101. (doi:10.1088/1751-8113/48/10/105101)

61. Clusella P, Politi A, Rosenblum M. 2016 A minimal model of self-consistent partial synchrony. *New J. Phys.* **18**, 093037. (doi:10.1088/1367-2630/18/9/093037)

62. Daido H. 1992 Order function and macroscopic mutual entrainment in uniformly coupled limit-cycle oscillators. *Progress Theoret. Phys.* **88**, 1213–1218. (doi:10.1143/ptp/88.6.1213)

63. Daido H. 1994 Generic scaling at the onset of macroscopic mutual entrainment in limit-cycle oscillators with uniform all-to-all coupling. *Phys. Rev. Lett.* **73**, 760–763. (doi:10.1103/PhysRevLett.73.760)

64. Crawford JD, Davies KTR. 1999 Synchronization of globally-coupled phase oscillators: singularities and scaling for general couplings. *Phys. D Nonlinear Phenom.* **125**, 62. (doi:10.1016/S0167-2789(98)00235-8)

65. Chialvo DR. 2010 Emergent complex neural dynamics. *Nat. Phys.* **6**, 744. (doi:10.1038/nphys1803)

66. Nordham CA, Tognoli E, Fuchs A, Kelso JAS. 2018 How interpersonal coordination affects individual behavior (and vice versa): experimental analysis and adaptive HKB model of social memory. *Ecol. Psychol.* **7413**, 1–26. (doi:10.1080/10407413.2018.1438196)

67. Bowman AW, Azzalini A. 1997 *Applied smoothing techniques for data analysis*. New York, NY: Oxford University Press.

68. Hogg RV. 1979 Statistical robustness: one view of its use in applications today. *Amer. Stat.* **33**, 108–115. (doi:10.2307/2683810)

Supplementary Materials

For the article "**Connecting empirical phenomena and theoretical models of biological co-ordination across scales**" by Mengsen Zhang, Christopher Beetle, J. A. Scott Kelso and Emmanuelle Tognoli, in the Journal of the Royal Society Interface.

Additional analyses on the coexistence of inphase and antiphase preference

The coexistence of inphase and antiphase preference in human coordination (24) (Fig 2D-F) and model behavior (Fig 5D-F) is reflected by the location of troughs (minima in the probability density functions) separating the inphase and antiphase peaks. In the human data (Fig 2D-F), the minima are at $\phi = 0.62\pi$, 0.77π, and 0.8π (away from both 0 and π) for $\delta f = 0, 0.3$, and 0.6 Hz respectively, with the minimum for $\delta f = 0$ Hz significantly less than chance ($p < 0.0005$, Fig S1A; nowhere with probability density significantly less than chance for $\delta f = 0.3$, and 0.6 Hz, as shown in Fig S1BC). This suggests that there is an unstable phase relation between inphase and antiphase, which is most prominent for $\delta f = 0$ Hz. This is well reflected in the behavior of the present model (i.e. equation (3) with $a = b = 0.105$) shown in Fig 5D-F, where the minima of the probability density functions are at $\phi = 0.6\pi, 0.7\pi$, and 0.67π for $\delta f = 0, 0.3$, and 0.6 Hz and the contrast between the minimum and the antiphase peak is most prominent for $\delta f = 0$ Hz (Fig 5D). On the other hand, for the Kuramoto model (i.e. equation (3) with $b = 0$), the minima of the probability density functions are always at $\phi = \pi$ for all δf's (Fig 5G-I), reflecting the instability related to antiphase when second order coupling is removed (supported by analytical results in Section Multistability of the present model). To think probablistically of how the troughs in the distributions inform us about which model better captures empirical phenomena, we consider the probability of observing the minima of three random distributions in a specific interval. The probablity of the minima of three random distributions to fall within the interval $[0.6\pi, 0.8\pi]$ (like those for the human data and simulations of the proposed model)

is 0.008, and that for interval $[0.99\pi, \pi]$ (like those for simulations of the Kuramoto model) is 10^{-6}. Thus, the convergence between human behavior and that of the proposed model, the divergence between human behavior and the Kuramoto model are highly unlikely to be due to chance. With all considered, the experimental phenomena from (24) cannot be fully captured without the second order coupling.
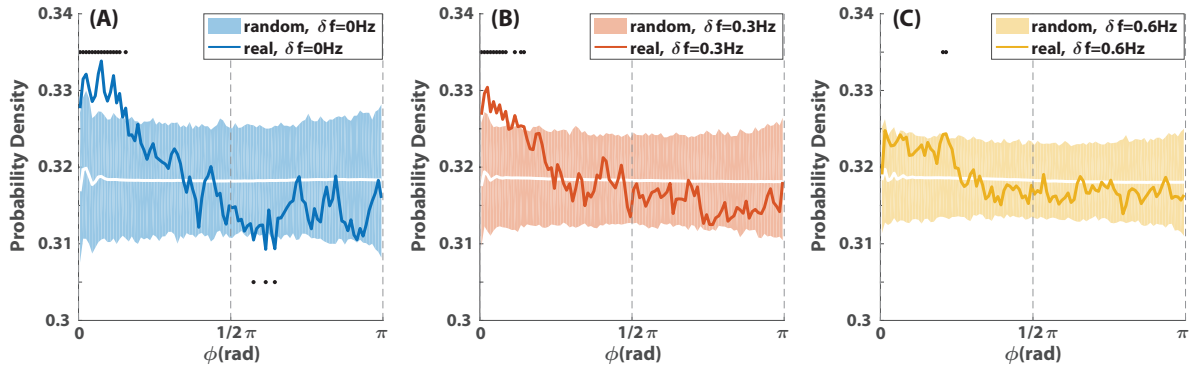

Fig S1. Relative phase distributions in the human experiment and comparisons with corresponding chance-level distributions for $\delta f = 0$ (A), 0.3 (B), and 0.6 Hz (C). coloured solid lines are the probability density functions of all dyadic relative phases for different δf's, each estimated in 100 bins. White solid lines and colour-shaded areas are the chance level distributions and corresponding confidence intervals with significance level $p = 0.0005$ per bin (after Bonferroni correction for $\hat{p} = 0.05$ for an entire distribution; see the construction of random distributions in Section D in S1 File of (24)). Black dots above the distributions mark where the probability density functions are significantly greater than chance, and black dots below mark where they are significantly less than chance (dots appear as bars when significant difference from chance is found in consecutive bins). This is a reproduction of Fig E (B1-B3) in S1 File of (24) but with all bins significantly different from chance marked (rather than as in (24), bins were marked only if significance was found in 3 or more consecutive bins).

For simulated dynamics, we show in Fig S2 that antiphase peaks in the relative phase distributions (prominent in Fig S2A, weak in Fig S2BC, which were reproduced from Fig 5D-F) did not result from transient behavior. Removal of transients from every simulated trial has little effect on the the relative phase distributions (comparing red dashed curves to black solid curves).
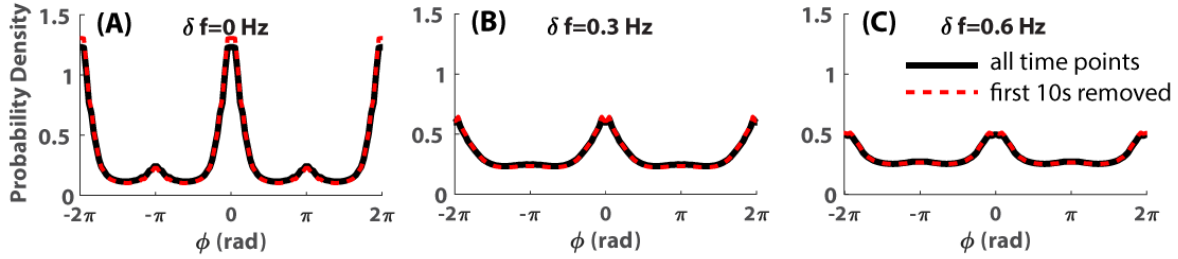
Fig S2. Aggregated relative phase distributions of simulated trials with $\delta f = 0$ (A), 0.3 (B), and 0.6 Hz (C). Each distribution was computed from 200 simulated time series. Distributions computed from all time points of all trials are plotted as black solid curves, which are identical to those in Fig 5D-F. Distributions computed from the same trials but with the first 10s of each time series discarded are plotted as red dashed curves.

Choosing the appropriate coupling strength

What we want to see is how the present model behaves as we manipulate the diversity of natural frequency ω_i's just as we did to human subjects. However, there remain two unknown parameters to be taken care of, namely the coupling strength a and b in equation (3). Before systematically finding the appropriate coupling strength, we want to first show qualitatively how it affects the dynamics.

Three simulated trials with increasing coupling strength are shown in Fig 4 from A to C, where the initial phases and natural frequencies are the same across trials (warm-color group centered around $f_A = 1.2$ Hz, cold-color group $f_B = 1.8$ Hz, corresponding to the condition $\delta f = 0.6$ Hz). When the coupling is weak ($a = b = 0.1$, Fig 4A), oscillators are well-segregated into two frequency groups. Within each frequency group, members intermittently converge (marked by black triangles) then diverge, reflecting metastability at a group level (collective dwells). For intermediate coupling ($a = b = 0.2$, Fig 4B), oscillators within each group are locked together, interacting strongly as a whole with the other frequency group (seen as the oscillation of frequency), so that the ensemble ($N = 8$) behaves like a dyad ($N = 2$). Finally, for strong coupling ($a = b = 0.4$, Fig 4C), everyone converges to a single steady frequency.

3

We see a progression from group-level segregation to integration from (A) to (C), indicating the important role of coupling strength in determining intergroup relation. Qualitatively, the model's behavior under weak coupling (Fig 4A) is closer to human behavior (Fig 2C) than that of stronger coupling. Next we take a more quantitative look.

To quantify the joint effect of frequency diversity (δf) and coupling strength ($a = b$ for simplicity) on integration and segregation between two frequency groups, we calculated the level of intergroup integration (β_1) for simulated trials using the same method as for the human experiment (see Phase-locking value and level of integration in Materials and Methods in the main text). For each parameter pair ($\delta f, a$) with $a = b$, we simulated 200 trials. In each simulated trial, two frequency groups A and B each consists of four oscillators ($\varphi_1, \cdots, \varphi_4$ in group A, $\varphi_5, \cdots, \varphi_8$ in group B). The natural frequency of oscillators in group A (i.e. $\omega_1, \cdots, \omega_4$, divided by 2π) was drawn from a distribution $P(f_A)$ centered around f_A (corresponds to the metronome frequency for the group in the human experiment), and $P(f_B)$ for group B. The difference between two groups $\delta f = |f_A - f_B|$ corresponds to the level of diversity in the human experiment. Here the probability density function $P(f)$, which defines frequency dispersion within each group, was obtained by a nonparametric estimation of the empirical distribution (see Materials and Methods in the main text).

The level of intergroup integration for simulated trials is shown in Fig 4D as the colour of each pixel (diversity δf as y-coordinate; coupling strength $a = b$ as x-coordinate). Three regimes are apparent: the highly integrated (yellow, $\beta_1 \approx 1$), the partially integrated (red, $0 < \beta_1 \ll 1$), and the segregated (blue, $\beta_1 < 0$). Between the red and blue area is the critical boundary (white solid line, $\beta_1 = 0$), separating the regimes of integration and segregation. With any fixed coupling strength, for the critical boundary to fall between $\delta f = 0.3$ Hz and $\delta f = 0.6$ Hz as in the human experiment, the coupling strength has to be weak (for $\delta f = 0.6$ Hz, $\beta_1 < 0$ only when $a = b < 0.15$) but not too weak (for $\delta f = 0.3$ Hz, $\beta_1 > 0$ only when $a = b > 0.05$).

Without risking overfitting, we simply choose the coupling strength $a = b = 0.105$, for which the level of intergroup integration is the closest to experimental observation for $\delta f = 0.3$ Hz ($\beta_1 = 0.31$).

Empirical distribution of tapping frequency around metronome frequency

In the "Human Firefly" experiment (24), subjects' tapping frequency during the transient between pacing and interaction (a proxy to "natural frequency"; see Materials and Methods in main text) dispersed around the metronome frequencies. The distribution of this deviation from metronome frequencies is shown in Fig S3 (blue histogram). Most of the time, subjects were very close to the metronome frequency (peak around zero). We can use a normal distribution $\mathcal{N}(\mu, \sigma)$ to capture this peak (Fig S3 yellow line), where parameters $\mu = 0$ and $\sigma = 0.0986$ (Hz) were estimated using the median and 10th percentile of the empirical distribution. We can see a difference between the empirical distribution and the normal distribution - the normal distribution (yellow line) does not capture the fat-tails of the empirical distribution (blue bars exceed yellow line on its shoulders). These "mutant fireflies" making up the fat-tails are not to be dismissed as out-liers, because they contribute to the behavior of others in the ensemble. To better represent the empirical distribution, we used Kernel Density Estimation (with a normal kernel) as described in section Estimating the distribution of natural frequencies of Materials and Methods in the main text, and the result of estimation is shown as the red line in Fig S3 (named kernel distribution). The kernel distribution better captures the tails of the empirical distribution and was used to generate natural frequencies of oscillators in the simulations.
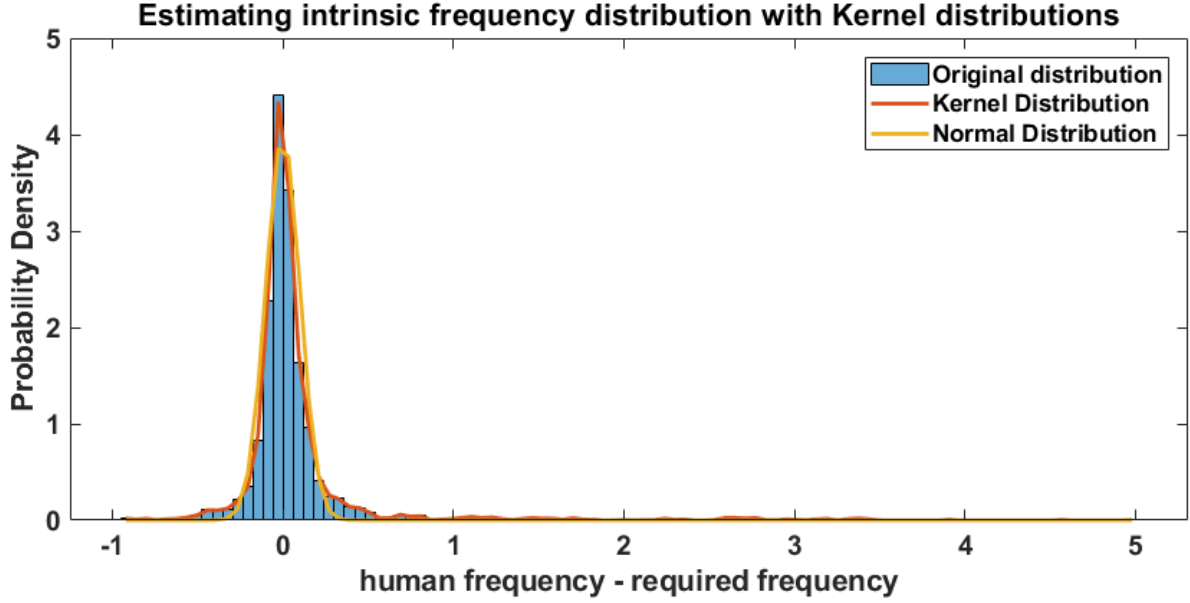
Fig S3. Distribution of human movement frequency around metronome frequencies and its estimation.

Examples of dynamics with intergroup coupling removed

By removing intergroup coupling, we obtain a modification of equation (3)

$$\dot{\varphi}_i = \omega_i - a \sum_{j=1}^{N} e_{ij} \sin \phi_{ij} - b \sum_{j=1}^{N} e_{ij} \sin 2\phi_{ij} \tag{S1}$$

where $e_{ij} = 1$ if $i, j \in \{1, 2, 3, 4\}$ or $i, j \in \{5, 6, 7, 8\}$, $e_{ij} = 0$ otherwise, for $N = 8$. The resulting dynamics (with all other parameters the same as examples in Fig 5A-C in the main text) are given in Fig S4. Within each frequency group (one group in cold colours, one group in warm colours), we see the same intragroup metastable dynamics being repeated regardless of intergroup difference ($df = 0, 0.3, 0.6$ Hz for Fig S4A, B, C respectively). These trials, without intergroup coupling, provide a baseline dynamics for comparison with Fig 5A-C, revealing the effect of intergroup influence. It turns out that for a given intragroup coupling, intragroup metastability comes from intragroup dispersion of natural frequencies. Metastability vanishes when two metastable groups have no intergroup difference (Fig 5A). In other words, without

intergroup difference ($\delta f = 0$), there are more oscillators within the same range of frequency, which cooperatively increases intragroup coordination. If we remove this intragroup dispersion of natural frequency (along with the metastability), we can no longer reproduce the experimental observation that intragroup coordination was weakened and altered by intergroup differences (see Effect of reduced intragroup variability in natural frequency for a statistical analysis).
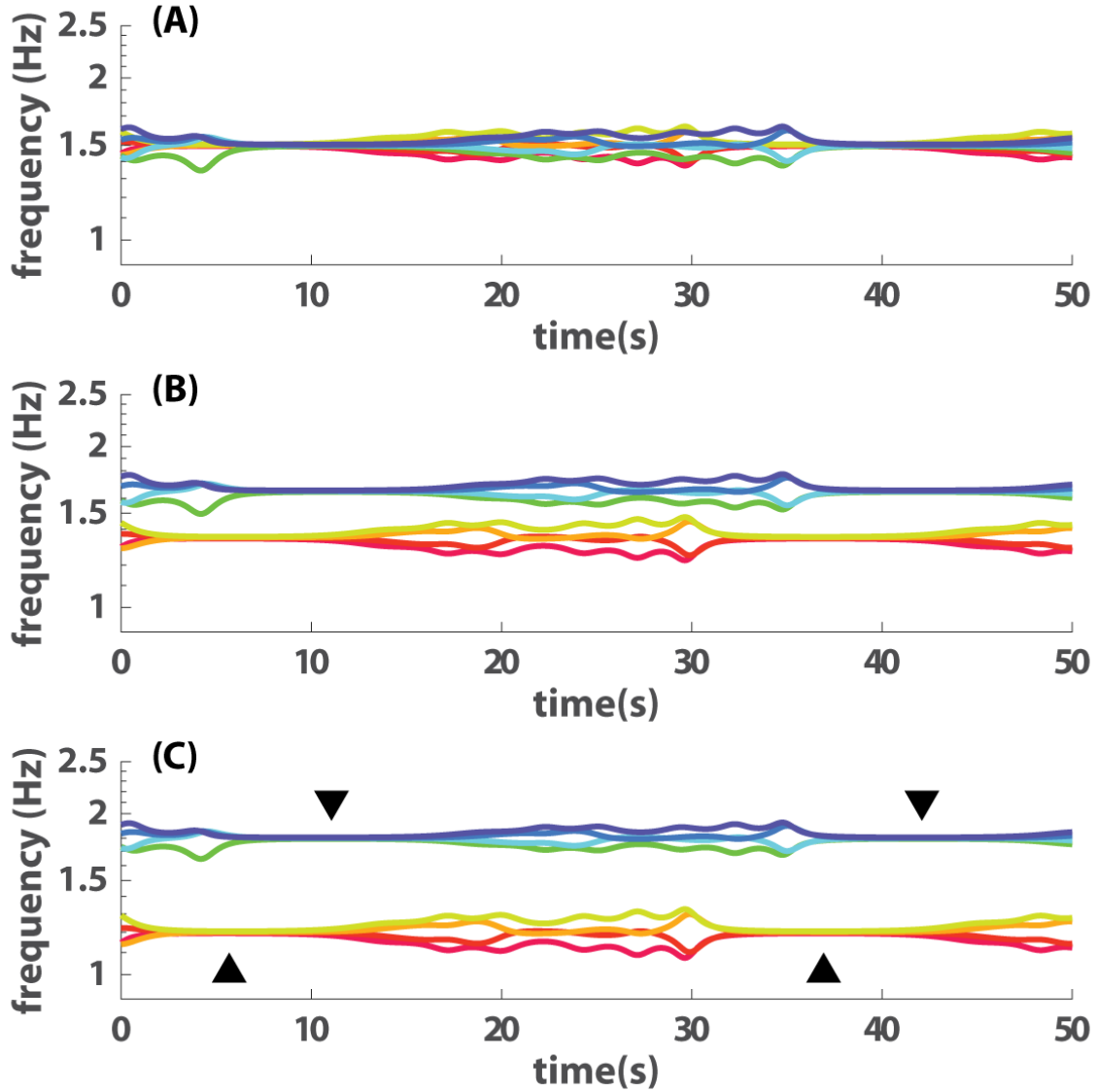
Fig S4. Intragroup dynamics without intergroup coupling, for intergroup difference $\delta f = 0$ (A), $\delta f = 0.3$ (B), and $\delta f = 0.6$ Hz (C).

With intergroup coupling, the time scale of metastability is modified by δf, as shown in Fig 5BC where the interval between two episodes of convergence (black triangles) is shorter for $\delta f = 0.3$ Hz (B) than for $\delta f = 0.6$ Hz (C). In Fig S5A, this is also visualized as the dynamics of phase-locking value (PLV) within groups (average PLV of all intragroup dyads in

3-s windows). When oscillators within groups converge, PLV is close to 1, and the interval between two consecutive peaks in a PLV trajectory reflects the time scale of the metastable coordination. Without influence from the other group, the time scales are exactly the same (trajectories exactly on top of each other in Fig S5B). With influence from the other group, the time scale depends on the level of intergroup difference (inter-peak intervals for $\delta f = 0.3$ Hz was much shorter than that of $\delta f = 0.6$ Hz in Fig S5A). Perhaps, we can consider $\delta f = 0$ Hz (i.e. lost of metastability, S5A blue line) as the special case where the inter-convergence interval is zero.
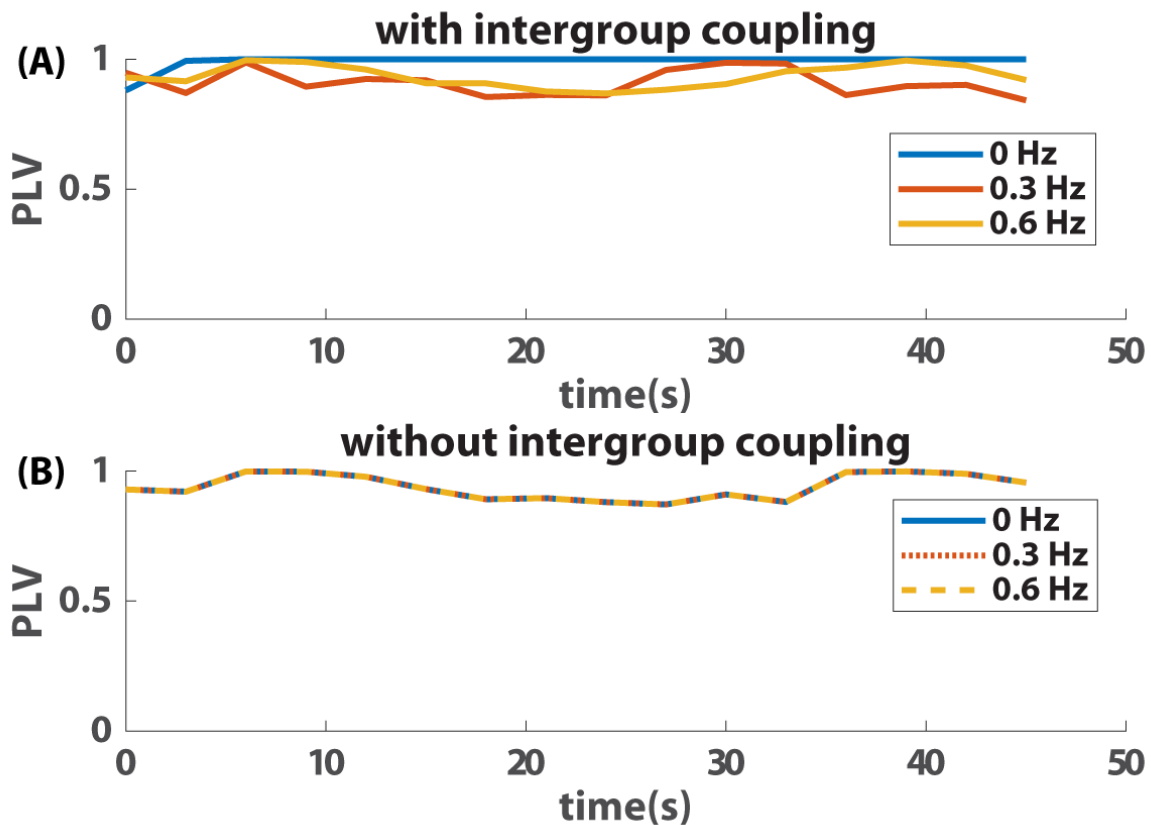

Fig S5. Dynamics of intragroup phase-locking value (PLV) with (A) and without (B) intergroup coupling.

It is also interesting to notice that for $\delta f = 0.6$ Hz, the metastable time-scale of the trial with

intergroup coupling (Fig S5A yellow line) is very similar to that of the trial without intergroup coupling (Fig S5B yellow line). This may be connected to the fact that $\delta f = 0.6$ Hz (given $a = b = 0.105$) is in the regime of intergroup segregation. It is perhaps a hypothesis worth further investigation that the level of intergroup integration (as measured by β_1, see main text) reflects how the time scale of intragroup metastability was affected by intergroup difference. Here our discussion on these examples is only to provide an intuitive understanding of the dynamics.

Effect of reduced intragroup variability in natural frequency

Recall that the reduction in intragroup coordination shown in Fig 3D (left) was based on simulations with nontrivial dispersion in natural frequency within each group, reflecting the natural variability carried into the experiment by human subjects. What if we remove that intragroup dispersion? As shown in Fig S6A (left three bars), intragroup coordination becomes all very close to the maximal level (phase-locking value close to 1) for all diversity conditions (MANOVA interaction effect $F(2, 19194) = 50152$, $p < 0.001$); we no longer see the large drop in intragroup coordination as seen in Fig 3BD. Even if we break the symmetry in coupling strength (use equation (1) with random coefficients, instead of uniform coupling in equation (3); see Random coupling for details), the phenomenon is not recovered (Fig S6B very similar to A; MANOVA interaction effect $F(2, 19194) = 59678$, $p < 0.001$). By studying the model's behavior, we found that the reduction in intragroup coordination due to intergroup difference, as observed in the human experiment, mainly depends on asymmetry in natural frequency rather than coupling strength.
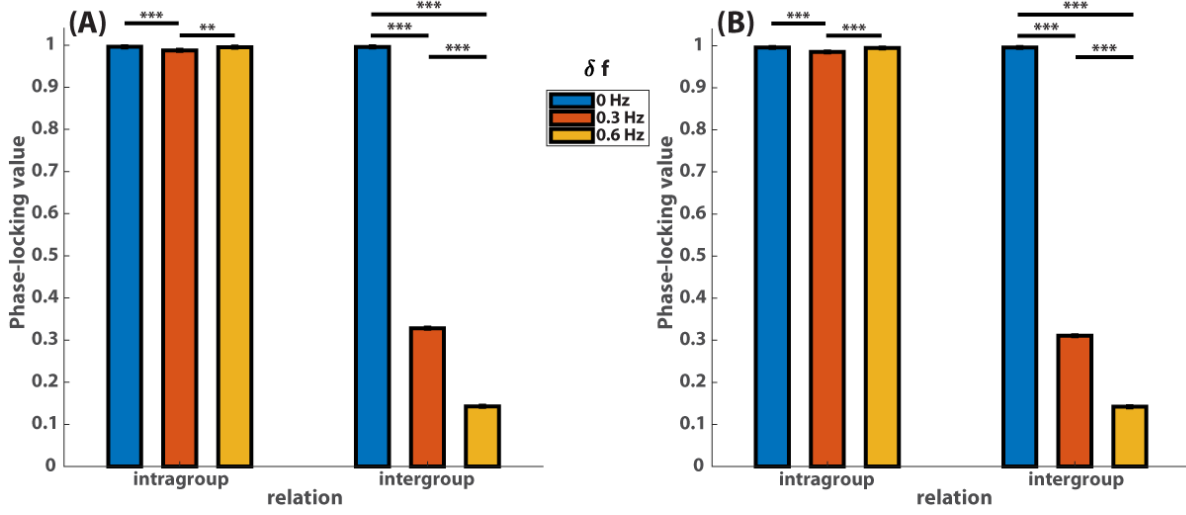
Fig S6. Intragroup and intergroup phase-locking by different levels of diversity δf for simulated data with identical natural frequency within groups. (A) shows the results of simulations with uniform coupling, and (B) non-uniform coupling (a's and b's are randomly distributed in the interval $[0, 0.2]$ see text for details).

Random coupling

To study the effect of symmetry breaking in coupling strength, we generated random coefficients for equation (1), following a uniform distribution on the interval $[0, a_{max}]$,

$$P(a) = \frac{1}{a_{max}}. \tag{S2}$$

We simulated 200 trials for each parameter pair $(\delta f = 0.3Hz, a_{max})$ for $a_{max} \in [0, 1]$ (discretized into intervals of length 0.01) with initial phases randomly distributed from 0 to 2π and natural frequencies following the empirical distribution from the human experiment (see Empirical distribution of tapping frequency around metronome frequency). We then find the value of $a_{max} = 0.2$, which produces the level of intergroup integration (β_1) closest to the experimental value (0.31). Using this fitted a_{max}, we simulated 200 trials with no intragroup dispersion in natural frequency, which were used to produce results in Fig S6B.

11

Intergroup relation without second order coupling

To examine whether the second order coupling term (i.e. $b \sum \sin 2\phi_{ij}$) in equation (3) is necessary for reproducing key experimental results, we let $b = 0$ and followed the exact same analysis as for the case of $b \neq 0$. The results are shown in Fig S7 (its $b \neq 0$ counterpart is Fig 4D), and Fig S8AB (its $b \neq 0$ counterpart is Fig 3CD).

Fig S7 shows the organization of the parameter space $\delta f \times a$ in terms of the level of integration between groups (β_1, see definition in main text). Similar to Fig 4D (for $b \neq 0$), the space consists of three regions - complete integration ($\beta_1 \approx 1$, yellow), partial integration ($0 < \beta_1 \ll 1$, red), and segregation ($\beta_1 < 0$, blue) - arranged from upper right to lower left. Fig S7 is approximately a scaled version of Fig 4D along a.
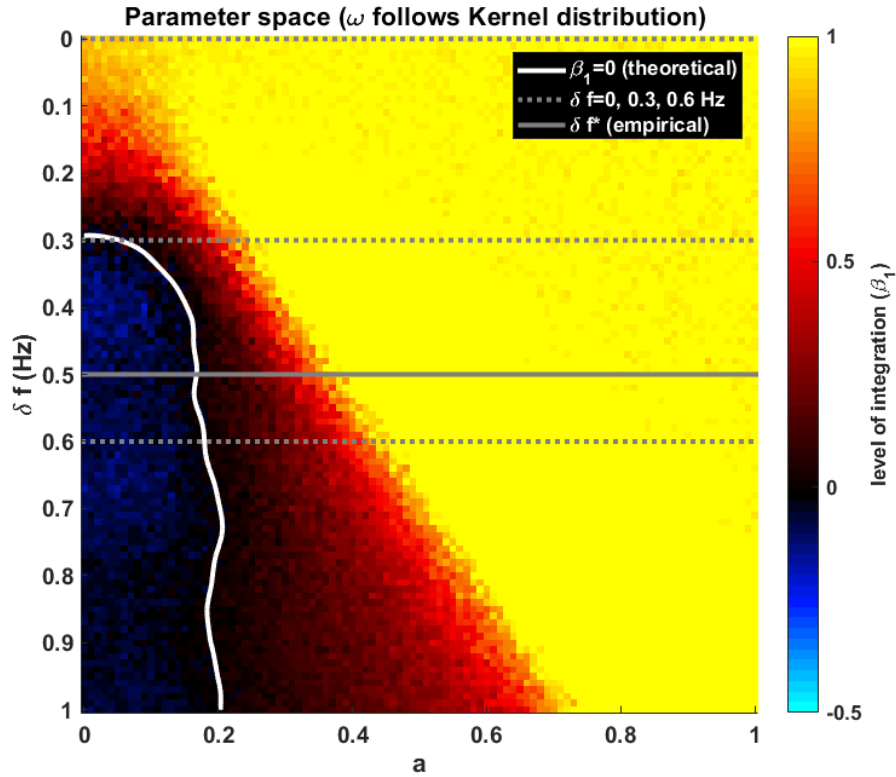

Fig S7. Level of integration between groups by δf and a, with $b = 0$.

We estimated the coupling strength to be $a = 0.154$, where the corresponding level of intergroup integration for $\delta f = 0.3$ Hz is the closest to the empirical value (up to 10^{-3} precision for a; for $a = 0.154$, $\beta_1(0.3Hz) = 0.29$, the empirical value is 0.31). The corresponding relations between intragroup and intergroup coordination is shown in Fig S8A and average intra/intergroup coordination in Fig S8B for different levels of δf.

In Fig S8A, each dot represents a particular trial with its x-coordinate indicating the average intragroup coordination (measured by phase-locking value, see Materials and Methods in main text) and y-coordinate the average intergroup coordination, whereas the colour indicates the diversity δf. Similar to the human experiment and the case of $b \neq 0$, more intragroup coordination is associated with more intergroup coordination (i.e. intergroup integration) for $\delta f = 0$ and 0.3 Hz (blue, red regression lines with positive slopes), and less intergroup coordination (i.e. intergroup segregation) for $\delta f = 0.6$ Hz (yellow regression line with negative slope). Two differences are (1) the β_1 for $\delta f = 0.6$ Hz and $b = 0$ is not significantly different from zero ($p > 0.05$; see main text for more statistics), where as its counterparts in the human data and the case of $b \neq 0$ are ($p < 0.05$); (2) in the human data and the case of $b \neq 0$, three regression lines intersect at almost the same point (see Fig 3A, C), which is not the case for $b = 0$ (Fig S8A).
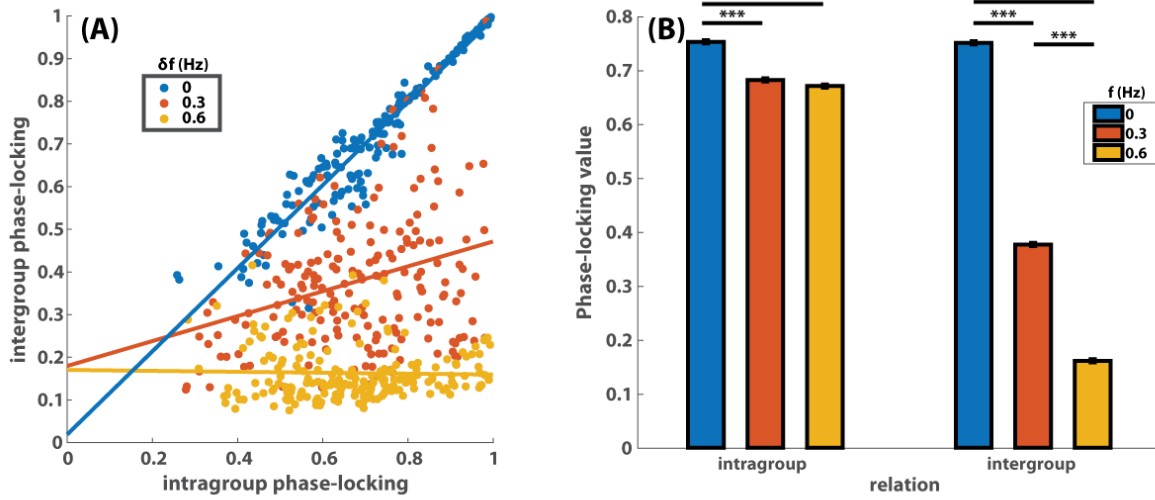
Fig S8. Intragroup, intergroup coordination and the relationship between them for $a = 0.154$ and $b = 0$. Here the level of coordination is measured by phase-locking value (see main text for definitions). (A) shows the relationship between intragroup (x-coordinate of each dot) and intergroup coordination (y-coordinate of each dot) for different levels of diversity (color code). The solid lines are corresponding regression lines whose slope quantifies the level of integration between two frequency groups. (B) shows the average intragroup (left three bars) and intergroup coordination (right three bars) for different levels of diversity (color code).

In Fig S8B, we show the average level of intragroup and intergroup coordination (again, in terms of phase-locking values). Intragroup coordination is reduced by the presence of intergroup difference (red, yellow bars on the left significantly shorter than blue bar). Intergroup coordination is more dramatically reduced by intergroup difference. Overall, these results resemble those of the human data and the case of $b \neq 0$.

Multistability of the present model

The equations for N Kuramoto oscillators with the same natural frequency, coupled to one another with a uniform coupling $a > 0$ are

$$\dot{\varphi}_i = -a \sum_j \sin(\varphi_i - \varphi_j). \tag{S3}$$

14

These equations can be recast in the mean-field form

$$\dot{\varphi}_i = -r\sin(\varphi_i - \psi) \qquad \text{with} \qquad r\,e^{i\psi} := a\sum_j e^{i\varphi_j}, \tag{S4}$$

which admit two types of fixed points: either **(a)** $r = 0$, or **(b)** $\sin(\varphi_i - \psi) = 0$ for each oscillator. In either case, the linearized equations governing the evolution of a small perturbation $\delta\varphi$ away from a fixed point are

$$\begin{aligned}
\delta\dot{\varphi}_i &= -a\sum_j \cos(\varphi_i - \varphi_j)\,(\delta\varphi_i - \delta\varphi_j) \\
&= -r\cos(\varphi_i - \psi)\,\delta\varphi_i + a\sum_j \cos(\varphi_i - \varphi_j)\,\delta\varphi_j
\end{aligned} \tag{S5}$$

We will study these linearized equations in the two cases separately.

Case (a) The first term of equation (S5) vanishes in this case. If we assume further that $\delta\varphi_j = 0$ initially for all but one oscillator, then the simplified equations are

$$\delta\dot{\varphi}_i = a\cos(\varphi_i - \varphi_j)\,\delta\varphi_j. \tag{S6}$$

In particular, $\delta\varphi_j$ itself grows exponentially at a rate a, so this fixed point cannot be stable.

Case (b) In this case there are two subgroups of oscillators, all exactly inphase within their group, and exactly antiphase to the other group. These groups cannot be equal in number because then $r = 0$ in equation (S5). Accordingly, we have $r = (n_+ - n_-)a$, where $n_+ > n_-$ are the sizes of the in- and antiphase groups (relative to the mean oscillator ψ, which of course is inphase with the larger group). The linearized equations become

$$\delta\dot{\varphi}_i = -(n_+ - n_-)as_i\,\delta\varphi_i + as_i\sum_j s_j\,\delta\varphi_j, \tag{S7}$$

where $s_i := \cos(\varphi_i - \psi) = \pm 1$ indicates whether φ_i is in- or antiphase to ψ. This equation can be recast in the matrix form

$$\delta\dot{\varphi} = J\,\delta\varphi := \left[aSHS - (a\,\mathrm{tr}\,S)S\right]\delta\varphi, \tag{S8}$$

15

where S is the $N \times N$ matrix with non-zero entries $s_i = \pm 1$ along the diagonal and H is the $N \times N$ matrix with all entries equal to $+1$. Our goal is to show that the Jacobian matrix J has at least one positive eigenvalue. This will imply that the fixed point is unstable dynamically. To do this, first we use the elementary identities $S^2 = 1$ and $H^2 = (\operatorname{tr} 1)H$ to calculate

$$J^2 = (a \operatorname{tr} 1)J - (a \operatorname{tr} S)\big[aHS + aSH - (a \operatorname{tr} 1)S - (a \operatorname{tr} S)1\big], \qquad \text{(S9)}$$

where 1 denotes the $N \times N$ identity matrix. The additional identity $HSH = (\operatorname{tr} S)H$ then gives

$$J^3 = (a \operatorname{tr} 1)J^2 + (a \operatorname{tr} S)^2 J + (a \operatorname{tr} S)^2\big[aH - (a \operatorname{tr} 1)1\big] \qquad \text{(S10)}$$

Applying all three of these identities one last time yields

$$J^4 = (a \operatorname{tr} 1)J^3 + (a \operatorname{tr} S)^2 J^2 - (a \operatorname{tr} 1)(a \operatorname{tr} S)^2 J. \qquad \text{(S11)}$$

That is, J solves a quartic polynomial, which moreover factors in the form

$$J\big[J - (a \operatorname{tr} 1)1\big]\big[J - (a \operatorname{tr} S)1\big]\big[J + (a \operatorname{tr} S)1\big] = 0. \qquad \text{(S12)}$$

This is clearly the minimal-order polynomial that J solves, and it has all distinct roots. It follows that J has a complete basis of eigenvectors with eigenvalues $\lambda_0 := 0$, $\lambda_* := Na$, $\lambda_+ := (n_+ - n_-)a$, and $\lambda_- := (n_- - n_+)a$. (We can't tell the multiplicity of each of these eigenvalues from this calculation, but each has at least a one-dimensional eigenspace associated to it.) The zero eigenvalue arises because the right side of equation (S3) involves only *relative* phases, so the dynamics is insensitive to rigid rotations $\varphi_i \mapsto \varphi_i + \theta$ for all i. The eigenvalues λ_* and λ_+, meanwhile, are strictly positive, and show that this fixed point is unstable.

The lone exception to this argument occurs when $n_- = 0$, and therefore $S = 1$. Then we have $J = a[H - N1]$, which clearly has a zero eigenspace corresponding to the rigid rotation of all oscillators in the system (*i.e.*, all $\delta\varphi_i$ equal to one another). Apart from this, there is

only a single, complementary eigenspace of dimension $N - 1$ associated with the eigenvalue $\lambda = -Na$. The configuration with all oscillators exactly inphase is therefore the *only* stable fixed point solution of the Kuramoto model.

Our model (with second-order coupling), on the other hand, has multiple stable fixed points for suitable values of its parameters. For uniformly coupled, identical oscillators, our equations are

$$\dot{\varphi}_i = -a \sum_j \sin(\varphi_i - \varphi_j) - b \sum_j \sin 2(\varphi_i - \varphi_j). \tag{S13}$$

The fixed points of the Kuramoto model with each φ_i equal either to ψ or to $\psi + \pi$ are also fixed points of these equations, and the linearized equations around such a fixed point are

$$\delta\dot{\varphi}_i = -(n_+ - n_-)a s_i\, \delta\varphi_i + a s_i \sum_j s_j\, \delta\varphi_j - 2Nb\, \delta\varphi_i + 2b \sum_j \delta\varphi_j. \tag{S14}$$

Here again we set $s_i := \cos(\varphi_i - \psi) = \pm 1$ and let $n_\pm$ denote the numbers of oscillators with $s_i = \pm 1$. The matrix form of these linearized equations is

$$\delta\dot{\varphi} = J\, \delta\varphi := \left[aSHS - (a \operatorname{tr} S)S + 2bH - (2b \operatorname{tr} 1)1 \right] \delta\varphi, \tag{S15}$$

where the matrices S, H, and 1 are defined as before. This Jacobian matrix differs from the Kuramoto Jacobian, which now we denote J_a, by its last two terms. Importantly, we have

$$J_a H = aSHSH - (a \operatorname{tr} S)H = 0 \tag{S16}$$

because $HSH = (\operatorname{tr} S)H$. It follows that all cross-terms vanish in any binomial expansion:

$$\left[J + (2b \operatorname{tr} 1)1 \right]^n = \left[J_a + 2bH \right]^n = J_a^n + \left[2bH \right]^n \tag{S17}$$

for all integers n. Applying these results in equation (S10) then shows that

$$\left[J + (2b \operatorname{tr} 1) \right]^3 - (a \operatorname{tr} 1)\left[J + (2b \operatorname{tr} 1) \right]^2$$
$$- (a \operatorname{tr} S)^2 \left[J + (2b \operatorname{tr} 1) \right] + (a \operatorname{tr} S)^2 (a \operatorname{tr} 1)1$$
$$= (a \operatorname{tr} S)^2 aH + \left[2bH \right]^3 - (a \operatorname{tr} 1)\left[2bH \right]^2 - (a \operatorname{tr} S)^2 \left[2bH \right]. \tag{S18}$$

Each term on the right here vanishes if we multiply through by J. Meanwhile, the cubic polynomial on the left is the same one from the Kuramoto case, with its argument shifted by $J \mapsto J + (2b \operatorname{tr} 1)1$. It factors in the same way as before to give the minimal polynomial

$$J\big[J + (2b \operatorname{tr} 1 - a \operatorname{tr} 1)1\big]\big[J + (2b \operatorname{tr} 1 - a \operatorname{tr} S)1\big]\big[J + (2b \operatorname{tr} 1 + a \operatorname{tr} S)1\big] = 0 \qquad \text{(S19)}$$

for the present model. The *non-zero* eigenvalues of the Kuramoto models are therefore all shifted by the same amount, giving $\lambda_0 = 0$, $\lambda_* = (a-2b)N$, and $\lambda_\pm := \pm(n_+ - n_-)a \operatorname{tr} S - 2Nb$. These are all negative as long as $2b > a$, the same condition that governs the HKB model for dyadic coordination. Our model is multistable when its parameters satisfy this condition.

Additional triadic dynamics

Here we provide in Fig S9 two additional variations of the simulated triadic dynamics shown in Fig 6B. Fig S9A shows what happens when all three oscillators have the identical coupling style, i.e. $a_1 = a_3 = a_4$ and $b_1 = b_3 = b_4$ (keeping the same mean coupling strength as Fig 6B and C). With the symmetry completed restored (in contrast to Fig 6C where only the symmetry between agent 3 and 4 is restored), not only the "bumps" in ϕ_{34} are gone but also the metastability altogether (at least at the observable time scale). This further illustrates the role of symmetry breaking in understanding the single-trial dynamics.
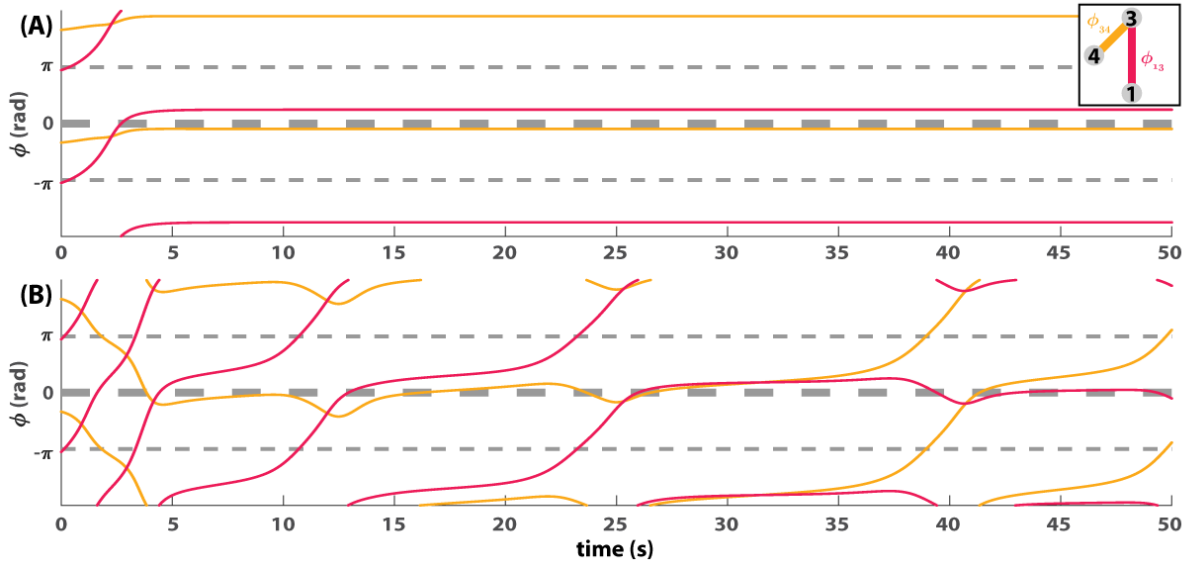
Fig S9. Simulated triadic coordination with (A) $a_1 = a_3 = a_4 = 0.4033$ and (B) varying natural frequency ω_3.

Fig S9B shows what happens when agent 3's natural frequency is not constant. A main clue suggesting a non-constant natural frequency is the increasing size of "bumps" in ϕ_{34} observed in the human behavior (see Fig 6A, the bump in yellow line at 15s was smaller than the one at 25s, and even smaller than the one at 37s) which was accompanied by growing length of the dwells in ϕ_{13} (red trajectory in Fig 6A has three periods of flattening, each one longer than the previous one). This could simply mean that agent 3's "natural frequency" was moving towards agent 1's and away from agent 4's. In the model, the natural frequencies of agent 1 and 4 are 1.57 and 1.45 Hz respectively. We simply let ω_3 increase linearly from 1.2 Hz to 1.7 Hz, instead of being constant (i.e. 1.375 Hz for Fig 6BC and S9A), over the course of the trial. The resulted dynamics is shown in Fig S9B. We see the dwells of ϕ_{13} (red line flattening around 7, 17 and 32s) are getting longer over time as the bumps in ϕ_{34} (yellow line) grow (the last bump grows out of itself at 37s and leaves inphase). In fact, at the end of the last dwell (around 37s) ϕ_{13} is no longer metastable in the original sense but begins to oscillate around inphase $\phi = 0$, whereas ϕ_{34} takes its place at that time and becomes metastable (i.e. after 37s yellow line starts

19

wrapping).

Gradually increasing natural frequency of agent 3 (ω_3) creates two subtle effects in addition to the increasing bump size. The first has already been hinted at that a gradual change of parameter can cause ϕ_{34} to suddenly leave inphase ($\sim$ 37s yellow line in Fig S9B). In the human trial (Fig 6A), ϕ_{34} had also, after the third bump, left inphase (37s). The difference is that the humans left for antiphase, instead of becoming metastable as for our simple model assuming linearly increasing natural frequency. This suggests that there was, unsurprisingly, more interesting adaptation going on in human movement frequency than just a linear ramping. Another subtle effect is of the same flavor but is concerned with what happens before ϕ_{34} began to dwell at inphase. In the human trial, ϕ_{34} decreased for almost one cycle before it stopped at inphase (0-10s yellow line in Fig 6A). This is not the case with constant frequency (Fig 6B, yellow line, ϕ_{34} immediately increases to inphase after the beginning of the trial), but it is the case with varying frequency (Fig S9B, yellow line, 0-5s). All these show by a very simple example how gradual adaptation in natural frequency may cause sudden changes in coordination patterns.

A note on metastability

For intuition, let us assume that there are N oscillators in a stationary organization defined by $N - 1$ relative phases, each of which remains near inphase, near antiphase, or wrapping, giving us $S = 3^{N-1}$ different stationary patterns for our model ($S = 2^{N-1}$ for the Kuramoto model because of the lack of antiphase). Now if we look at patterns as sequences of metastable dwells, we could have $M = \sum_{l=1}^{S} \frac{S!}{(S-l)!}$ patterns of various period l (with non-repeated spatial configurations in sequence). These of course are not all necessarily reachable by a system, which in itself is an interesting theoretical problem, but still the repertoire M is much greater than S. This thought experiment shows how metastability contributes to biological complexity

in a very significant way.

Design of the human experiment

The human experiment (24) was performed by a total of 120 subjects in 15 ensembles. Each ensemble completed 18 trials (6 trials for each condition $\delta f = 0, 0.3$ and 0.6 Hz) of interaction in a complete network, except one ensemble for which only 7 trials (2 for $\delta f = 0$ Hz, 2 for $\delta f = 0.3$ Hz, and 3 for $\delta f = 0.6$ Hz) were completed due to equipment malfunction. This yields 86 trials for $\delta f = 0$ Hz, 86 trials for $\delta f = 0.3$ Hz, and 87 trials for $\delta f = 0.6$ Hz. See (24) for additional details.